Ore Geology Reviews 92 (2018) 144–160

Contents lists available at ScienceDirect

Ore Geology Reviews

journal homepage: www.elsevier.com/locate/oregeorev

# A slab break-off model for the submarine volcanic-hosted iron mineralization in the Chinese Western Tianshan: Insights from Paleozoic subduction-related to post-collisional magmatism

Xin-Shui Wang[a], Xi Zhang[b], Jun Gao[a,c,*], Ji-Lei Li[a,f], Tuo Jiang[d], Sheng-Chao Xue[e]

[a] Key Laboratory of Mineral Resources, Institute of Geology and Geophysics, Chinese Academy of Sciences, 100029 Beijing, China
[b] China Minmetals Corporation, 100010 Beijing, China
[c] College of Earth Science, University of Chinese Academy of Sciences, 100049 Beijing, China
[d] Laboratory of Isotope Geochemistry, Wuhan Centre of China Geological Survey, 430205 Wuhan, China
[e] State Key Laboratory of Geological Processes and Mineral Resources, China University of Geosciences, Beijing 100083, China
[f] College of Earth Science and Engineering, Shandong University of Science and Technology, 266590 Qingdao, China

ARTICLE INFO

*Keywords:*
Volcanic-hosted iron deposits
Tectonic setting
Western Tianshan
Slab break-off
Central Asian Orogenic Belt

ABSTRACT

The distinct submarine volcanic-hosted iron ore deposits in the Awulale Iron Metallogenic Belt are the most important sources for iron in the Chinese Western Tianshan metallogenetic province, although, the exact tectonic setting for their formation remains poorly constrained. A compilation of published and new geochronological and geochemical data suggests a protracted magmatism from ca. 450 to 290 Ma was in close spatial and temporal proximity to the iron deposits. The different magmatic rocks have broadly similar arc-like geochemical signatures such as LREE and LILE enrichments, HREE and HFSE depletions, Nb–Ta–Ti negative anomalies and flat HREE patterns, all of which are attributed to magmatic differentiation and/or partial melting in relatively thin crust due to long-term extension. The contrasting whole-rock Nd isotopic patterns of the igneous rocks and the well-defined peak metamorphism (ca. 320–310 Ma) of the subduction-zone high-pressure rocks indicate that ca. 450–321 Ma magmatic rocks with an increasingly positive $\varepsilon_{Nd}(t)$ shift were formed during the northward subduction of the South Tianshan Ocean, where slab rollback resulted in an extensional setting in the southern Yili-Central Tianshan Block. In contrast, the synchronicity of the ca. 320–310 Ma subduction-zone peak metamorphism and magmatic flare-up with uniformly positive $\varepsilon_{Nd}(t)$ values is interpreted as the consequence of slab break-off subsequent to the oceanic subduction and the continental collision. By inference, the late-stage (ca. 309–290 Ma) magmatism was likely constructed in a post-collisional setting. The submarine volcanic-hosted iron mineralization exclusively occurred coeval with the peak metamorphism and intensive magmatism, probably suggesting slab break-off as the exact tectonic setting for iron mineralization. Consequently, the western extension of the Awulale Iron Metallogenic Belt occurring roughly parallel to the South Tianshan Orogen may have significant potential for prospecting the submarine volcanic-hosted iron ore deposits.

## 1. Introduction

The Central Asian Orogenic Belt (CAOB; Fig. 1a) is one of the largest and long-lived accretionary orogenic systems in the world, accompanied by voluminous magmatism and large-scale mineralization (Yakubchuk, 2004; Kröner et al., 2007; Xiao et al., 2015; Wan et al., 2017). Therefore, its complex geodynamic evolution and associated metallogeny have been in the research focus of many international geoscientists in the past decades. Currently, it is widely accepted that the CAOB was formed by sequential accretion of multiple microcontinents, island arcs, seamounts, oceanic plateaus and accretionary complexes as the result of the closure of the Paleo-Asian Ocean, thereby serving as an analogue for the architecture of the modern Southwestern Pacific archipelago (Wilhem et al., 2012; Wakita et al., 2013).

The Tianshan Orogen in the southwestern CAOB is regarded as hallmark of the final docking of the Tarim Craton with the Siberia Craton to the south during Paleozoic times (Fig. 1) and hence it is essential for unravelling the architectural framework of the southwestern CAOB. However, the tectonic evolution of the Tianshan Orogen is still controversial with respect to the subduction polarities of the oceanic basins and the timing of the collisions between different terranes (Gao et al., 2009; Charvet et al., 2011; Han et al., 2011; Wang et al., 2011a;

* Corresponding author at: Key Laboratory of Mineral Resources, Institute of Geology and Geophysics, Chinese Academy of Sciences, P.O. Box 9825, Beijing 100029, China.
*E-mail address:* gaojun@mail.iggcas.ac.cn (J. Gao).

https://doi.org/10.1016/j.oregeorev.2017.11.015
Received 15 June 2017; Received in revised form 18 October 2017; Accepted 15 November 2017
Available online 16 November 2017
0169-1368/ © 2017 Elsevier B.V. All rights reserved.

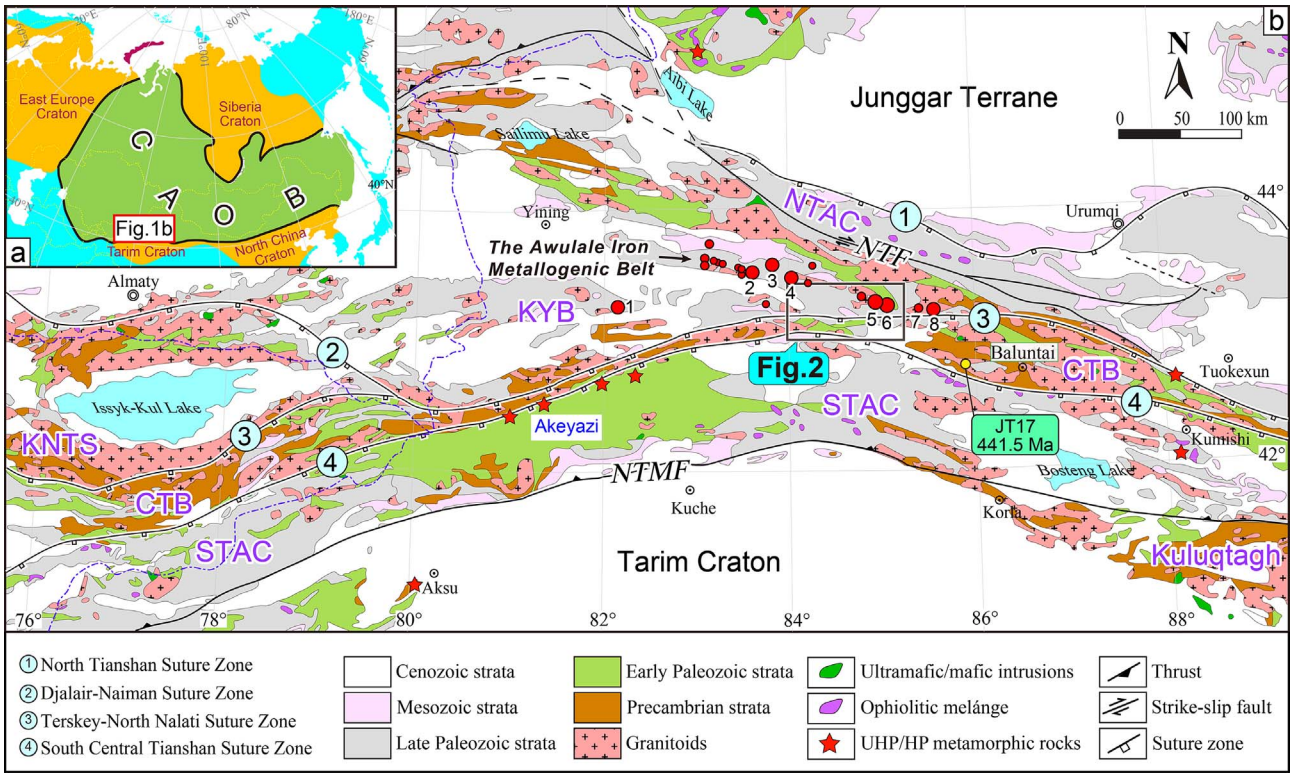


**Fig. 1.** (a) Tectonic outline of the Central Asian Orogenic Belt (CAOB) and environs (Xiao et al., 2013). (b) Simplified tectonic divisions of the Western Tianshan Orogen and adjacent areas (Gao et al., 2009; Wang et al., 2017). NTAC–North Tianshan Accretionary Complex, KYB–Kazakhstan–Yili Block, KNTS–Kyrgyzstan North Tianshan Block, CTB–Central Tianshan Block, STAC–South Tianshan Accretionary Complex. Major faults: NTF = North Tianshan Fault; NTMF = Northern Tarim Margin Fault. Note that the red circles denote the iron ore deposits in the Awulale Iron Metallogenic Belt including: 1–Kuolasayi, 2–Shikebutai, 3–Songhu, 4–Nixintage-Akesayi, 5–Chagangnuoer, 6–Zhibo, 7–Dunde, 8–Beizhan. One sample (JT17) outside the Fig. 2 is marked with zircon U–Pb age. (For interpretation of the references to colour in this figure legend, the reader is referred to the web version of this article.)

Xiao et al., 2013). This is largely due to the fact that in many previous studies geochemical characteristics of voluminous igneous rocks were employed as tracers for the geodynamic setting and tectonic evolution of the Western Tianshan Orogen (e.g., Xia et al., 2004; Dong et al., 2011; Long et al., 2011; Zhong et al., 2017). For example, trace element discrimination diagrams have been in widespread use and are regarded as an important tool to constrain the tectonic settings of granitic rocks, such as the plots of Rb–Y + Nb and Nb–Y (Pearce et al., 1984). Trace element compositional variations, nonetheless, are thought to be a function of the source characteristics and magmatic crystallization processes, while the tectonic setting is of secondary importance (Frost et al., 2001; Frost and Frost, 2008; Fiannacca et al., 2015). This is why post-collisional granitoids usually straddle over a range of fields in the discrimination diagrams since they are originated from a number of contrasting sources, depending on the thickness and composition of the crust during orogenesis (Pearce et al., 1984; Frost et al., 2001). Therefore, further comprehensive studies of Paleozoic igneous rocks in combination with regional geological evidence are required to readdress the tectonic evolution of the Tianshan Orogen.

The Chinese Western Tianshan hosts several large-medium submarine volcanic-hosted iron (both haematite and magnetite) deposits, such as Zhibo, Chagangnuoer, Beizhan, Dunde and Songhu, which constitute the Awulale Iron Metallogenic Belt (AIMB; Fig. 1b). The AIMB has more than 1.2 billion tons iron ore resources at an average grade of 40% (up to > 60%) and thus is thought to have an excellent prospecting potential for high-grade iron ore deposits in China (Zhang et al., 2014a,b). All the iron ore deposits are commonly hosted in Early Carboniferous submarine volcano-sedimentary rocks, represented by the widespread Dahalajunshan Formation (Zhang et al., 2012, 2014b, 2015). Based on geochronological and geochemical studies of the ore-related volcanic rocks and associated igneous rocks, various subduction-related tectonic settings such as continental arc (Zhang et al., 2012; Jiang et al., 2014b; Ge et al., 2015) and back-arc settings (Yan et al., 2015; Li et al., 2015b) are thought to have enhanced the iron mineralization, while continental rift related to mantle plume activities is an alternative (Xia et al., 2004). Hence, the exact tectonic setting of the submarine volcanic-hosted iron ore deposits remains to be elucidated in order to better understand the ore-forming process and to refine prospecting strategies for this type of iron ore mineralization.

In this study, we present new LA-ICP-MS zircon U–Pb ages, whole-rock major and trace element compositions and Sr–Nd isotopic data for Paleozoic igneous rocks in the AIMB and adjacent areas. In conjunction with published geochronological and geochemical data, we develop a slab break-off model to account for the formation of the submarine volcanic-hosted iron deposits in the Chinese Western Tianshan.

## 2. Geological background of the Chinese Western Tianshan

The Chinese Western Tianshan represents a Paleozoic orogenic collage formed by multiple subduction and accretion of several terranes between the Junggar Terrane and the Tarim Craton (Gao et al., 1998, 2009; Wang et al., 2008; Long et al., 2011; Xiao et al., 2013). Traditionally, it is divided into four tectonic domains from north to south, namely the North Tianshan Accretionary Complex, the Kazakhstan–Yili Block, the Central Tianshan Block and the South Tianshan Accretionary Complex (Fig. 1b; Gao et al., 2009; Xiao et al., 2013; Wang et al., 2014b).

The North Tianshan Accretionary Complex is exposed along the North Tianshan Fault or the Main Tianshan Shear Zone and mainly composed of late Carboniferous volcano-sedimentary rocks and ophiolitic slices formed by the subduction of the North Tianshan Ocean towards the south (e.g., Wang et al., 2006). Zircon U–Pb dating of gabbros and plagiogranites from the Bayingou ophiolite suggests that the North Tianshan Ocean existed at least between 344.0 ± 3.4 and

**Table 1**
Descriptions of the studied igneous rocks in the Awulale and adjacent areas.

| Sample No. | Rock type | Location | Coordinates | Mineral assemblages | Geochemical analyses |
|---|---|---|---|---|---|
| GL1 | Granodiorite | Qiaohuote Cu deposit | N43°5′29″, E84°24′6″ | Hbl (8–10%), Pl (35–40%), Kf (20–25%), Qtz (20–25%), minor Chl and Bt (3–5%) | GL1-1, -2, -3 |
| JT17 | Granodiorite | Eastern Haernuer | N42°47′18″, E85°5′10″ | Pl (50–55%), Kf (15–20%), Qtz (15–20%), Ep and Chl (5–10%) | JT17-1, -2, -3 |
| BY8 | Grantie | Bayinbuluke | N43°1′56″, E84°7′29″ | Kf (35–40%), Pl (30–35%), Qtz (20–25%), Bt + Chl + Ep (10–15%), accessory titanite and Fe-Ti oxides | BY8-1, -2, -3 |
| NESL2 | K-feldspar granite | Nuersala | N43°6′21″, E83°59′42″ | Kf (50–60%), Qtz (25–30%), Ser (10–15%), minor Ep | NESL2-6 |
| 10CG30 | Granodiorite | Huoshaoqiao | N43°11′56″, E84°59′21″ | Hbl (10–15%), Pl (40–45%), Kf (20–25%), Qtz (20–25%), minor Ep, Chl and Fe-Ti oxides (~5%) | 10CG30-3, -4, -5 |
| 12W20 | Diorite | Huoshaoqiao | N43°12′44″, E84°57′11″ | Hbl (40–50%), Pl (50–55%) | 12W20-1, -2, -3 |
| 12W19-4 | Diorite | Huoshaoqiao | N43°12′44″, E84°57′09″ | Hbl (25–30%), Pl (45–50%), Ep (10–15%), Chl (10–15%) | 12W19-5, -6, -7 |
| 10CG26 | Granodiorite | Chagangnuoer Fe deposit | N43°18′44″, E84°52′16″ | Hbl (15–20%), Pl (35–40%), Kf (20–25%), Qtz (20–25%), Fe-Ti oxides (~5%), minor Ep and Chl | 10CG26-1, -3, -6 |
| 10CG12 | Granite | Chagangnuoer Fe deposit | N43°12′19″, E84°53′28″ | Ep (20–25%), Pl (20–25%), Kf (20–25%), Qtz (20–25%), minor Chl | 10CG12-1, -2 |
| 10CG29 | Diorite | Gongnaisi | N43°15′48″, E84°37′50″ | Hbl (35–40%), Pl (40–45%), Qtz (5–10%), Fe-Ti oxides (10–15%) | 10CG29-1, -3, -4 |
| 0945 | Gabbro diorite | Zhibo Fe deposit | N43°19′56″, E84°1′34″ | Cpx (8–10%), Hbl (10–15%), Bt (10–15%), Pl (50–55%), Qtz (8–10%), minor Fe-Ti oxides (~2%) and Chl | 0945-1, -2, -3, -4 |
| Silurian volcanic rocks | Basalts, Basaltic andesites, Andesites | Qiaohuote Cu deposit | N43°5′56″, E84°35′22″ | Mainly Pl, Hbl and Cpx, minor Chl, Fe-Ti oxides and glasses | 0833-2, 0838-1, 0839-1, 0840-1, -2, -4, 0845-1, -2, 0846-1, -3, -6, -8 |

*Mineral abbreviations:* Cpx-clinopyroxene, Hbl-hornblende, Pl-plagioclase, Kf-K-feldspar, Qtz-quartz, Ep-epidote, Chl-chlorite, Bt-biotite, Ser-sericite.

324.8 ± 7.1 Ma (Xu et al., 2006; Li et al., 2015a) and that it was closed prior to ca. 316 Ma as evidenced by the Sikeshu stitching pluton (Han et al., 2010).

Bounded by the North Tianshan Fault to the north, the Kazakhstan-Yili Block (KYB) is a triangle-shaped area that wedges out eastwards (Fig. 1b). The KYB is regarded as a continental arc emplaced on a Precambrian basement, which consists of Meso- to Neoproterozoic gneisses and metasedimentary rocks (Gao et al., 2009; Wang et al., 2014a). The basement is covered by late Neoproterozoic to early Paleozoic passive margin sediments and late Ordovician to Carboniferous arc-related volcano-sedimentary rocks (e.g., Gao et al., 1998; Wang et al., 2014a). Voluminous intrusive rocks with ages of ca. 490–280 Ma were documented on both sides of the KYB and are thought to be arc-related or post-collisional associated with the subduction of the North Tianshan and/or the South Tianshan oceans beneath the KYB (e.g., Long et al., 2011; Wang et al., 2012; Zhong et al., 2017).

The Central Tianshan Block (CTB) is separated from the KYB by the North Nalati Fault (Fig. 1b), which was interpreted as the eastern extension of the Kyrgyz-Terskey suture zone (Nicolaev Line) in Kyrgyzstan and Kazakhstan (Lomize et al., 1997; Qian et al., 2009; Gao et al., 2015). The suture zone is further characterized by the ~470 Ma Makbal high-pressure metamorphic terrane (Meyer et al., 2013; Klemd et al., 2015), the late Cambrian–early Ordovician Terskey ophiolite (Lomize et al., 1997) and the 516.3 ± 7.4 Ma Xiate ophiolite intruded by the 470 ± 12 Ma collision-related diorite (Qian et al., 2009), all of which are interpreted as relics of the Terskey Ocean whose closure at ca. 470 Ma resulted in the collision of the KYB and the CTB (Qian et al., 2009). The CTB is an elongated microcontinent with a Neoarchean–Paleoproterozoic basement, represented by greenschist- to amphibolite-facies igneous rocks and metasediments (Wang et al., 2014b, 2017; Gao et al., 2015). Late Silurian arc-type volcanic and associated sedimentary rocks were thrust over the Precambrian basement and subjected to regional greenschist- to amphibolite-facies metamorphism and ductile deformation (Gao et al., 2009). In turn, both the basement and the late Silurian strata were unconformably overlain by unmetamorphosed Carboniferous subduction-related volcano-sedimentary rocks (Gao et al., 2009; Zhu et al., 2009). Paleozoic (ca. 480–260 Ma) granitoids and mafic intrusions are extensively exposed throughout the CTB and they were interpreted to be associated with the subduction of the Terskey Ocean or the South Tianshan Ocean and subsequent collision of the CTB and the Tarim Craton (e.g., Gao et al., 2009; Long et al., 2011; Ma et al., 2012).

The South Tianshan Accretionary Complex (STAC) is a wide tectonic zone between the CTB and the Tarim Craton, which is bounded by the Inylchek-Atbashi-South Nalati-Wuwamen fault to the north and the Northern Tarim Margin Fault to the south (Fig. 1b; Gao et al., 2009; Xiao et al., 2013). The STAC is mainly composed of the Akeyazi high-pressure metamorphic terrane, ophiolitic mélanges and coherent strata of imbricated late Ordovician–Carboniferous clastic sediments and limestones (Gao et al., 2009; Xiao et al., 2013; Jiang et al., 2014a). The northern ophiolite belt with ages of 439–332 Ma and mid-ocean ridge type affinity suggests that the South Tianshan Ocean lasted to the early Carboniferous, while the presence of the southern ophiolite belt with ages of 450–392 Ma and supra-subduction zone type affinity indicates the existence of a short-lived fore-arc basin during the southward subduction of the South Tianshan Ocean (Wang et al., 2011a; Jiang et al., 2014a). The Akeyazi terrane along the northern boundary has been extensively studied and the peak metamorphic ages are generally in consensus with a restricted range of 320–310 Ma (Fig. 9b; e.g., Su et al., 2010; Klemd et al., 2011; Li et al., 2011; Yang et al., 2013; Soldner et al., 2017; Tan et al., 2017), which was thought to represent the approximate time frame for the collision of the CTB and the Tarim Craton (e.g., Gao et al., 2011; Klemd et al., 2015; Li et al., 2016).

**Table 2**
Summary of sample localities, rock types and zircon U–Pb ages in the Awulale and adjacent areas.

| Sample NO. | Location | Rock type | Method | Age (Ma) | References |
|---|---|---|---|---|---|
| GL1 | Qiaohuote copper deposit | Granodiorite | LA-ICP-MS | 450.5 ± 1.5 | This study |
| JT17 | Eastern Haernuer | Granodiorite | LA-ICP-MS | 441.5 ± 1.1 | This study |
| BY8 | Bayinbuluke | Grantie | LA-ICP-MS | 434.6 ± 3.6 | This study |
| NESL2 | Nuersala | K-feldspar granite | LA-ICP-MS | 424.5 ± 1.4 | This study |
| 10CG30 | Huoshaoqiao | Granodiorite | LA-ICP-MS | 361.4 ± 0.94 | This study |
| 12W20 | Huoshaoqiao | Diorite | LA-ICP-MS | 354.3 ± 1.7 | This study |
| 12W19-4 | Huoshaoqiao | Diorite | LA-ICP-MS | 333.5 ± 2.1 | This study |
| 10CG26 | Chagangnuoer iron deposit | Granodiorite | LA-ICP-MS | 331.5 ± 0.91 | This study |
| 10CG12 | Chagangnuoer iron deposit | Granite | LA-ICP-MS | 327.5 ± 0.86 | This study |
| 10CG29 | Gongnaisi | Diorite | LA-ICP-MS | 324.4 ± 0.88 | This study |
| 0945 | Zhibo iron deposit | Gabbro diorite | LA-ICP-MS | 305.7 ± 0.88 | This study |
| K1-1305 | Xinyuan Forest Farm | Monzogranite | SHRIMP | 436 ± 8 | Zhu et al. (2006) |
| K1-9-17 | Quelute | Diorite | SHRIMP | 370 ± 7 | Zhu et al. (2006) |
| K1-14-17 | Quelute | Granite | SHRIMP | 366 ± 8 | Zhu et al. (2006) |
| 13ts14A | Haernuer | Granodiorite | LA-ICP-MS | 344 ± 3 | Zhong et al. (2017) |
| 13ts14B | Haernuer | Granite | LA-ICP-MS | 292 ± 5 | Zhong et al. (2017) |
| 13ts14I | Haernuer | Diorite | LA-ICP-MS | 353 ± 5 | Zhong et al. (2017) |
| 13ts15B | Haernuer | Monzogranite | LA-ICP-MS | 411 ± 4 | Zhong et al. (2017) |
| 13ts15C | Haernuer | Diorite | LA-ICP-MS | 421 ± 4 | Zhong et al. (2017) |
| 08XY1-1 | Qiakebu | Muscovite granite | LA-ICP-MS | 427.2 ± 5.7 | Xu et al. (2013) |
| 08XY2-1 | Qiakebu | Gabbro | LA-ICP-MS | 318.5 ± 2.6 | Xu et al. (2013) |
| 10QLT2-1 | Quelute | Muscovite granite | LA-ICP-MS | 357.2 ± 7.5 | Xu et al. (2013) |
| 10NLT1-1 | Nalati | Alkali grainte | LA-ICP-MS | 296.9 ± 2.4 | Xu et al. (2013) |
| 10NLT2-1 | Nalati | Gabbro | LA-ICP-MS | 340.2 ± 1.1 | Xu et al. (2013) |
| nlt01-1 | Northern Bayinbuluke | Diorite | LA-ICP-MS | 355 ± 9 | Zhu et al. (2012) |
| TS069 | Southern Xinyuan | Basalt | SHRIMP | 355.3 ± 2.4 | Zhu et al. (2009) |
| TS01 | Southern Xinyuan | Basalt | SHRIMP | 352.2 ± 3.2 | Zhu et al. (2009) |
| TS04 | Laerdundaban | Trachyandesite | SHRIMP | 324 ± 4.9 | Zhu et al. (2009) |
| TS1618 | Yuximolegai | Rhyolite | SHRIMP | 316 ± 2.5 | Zhu et al. (2009) |
| TS02 | Laerdundaban | Trachyandesite | SHRIMP | 312.8 ± 4.2 | Zhu et al. (2005) |
| DD-145 | Dunde iron deposit | Dacite | LA-ICP-MS | 316 ± 1.7 | Duan et al. (2014) |
| DD-117 | Dunde iron deposit | K-feldspar granite | LA-ICP-MS | 295.8 ± 0.71 | Duan et al. (2014) |
| 0939 | Zhibo iron deposit | Diorite | LA-ICP-MS | 318.9 ± 1.5 | Zhang et al. (2012) |
| 0947 | Zhibo iron deposit | Granite | LA-ICP-MS | 304.1 ± 1.8 | Zhang et al. (2012) |
| 0941 | Zhibo iron deposit | Granite | LA-ICP-MS | 320.6 ± 2.5 | Zhang et al. (2012) |
| 0943 | Zhibo iron deposit | Granite | LA-ICP-MS | 294.5 ± 1.6 | Zhang et al. (2012) |
| 10ZB04 | Zhibo iron deposit | Magnetite ore | LA-ICP-MS | 350 ± 2 | Zhang et al. (2015) |
| 10CG21 | Chagangnuoer iron deposit | Rhyolite | LA-ICP-MS | 321 ± 2 | Zhang et al. (2015) |
| 10CG04 | Chagangnuoer iron deposit | Granite | LA-ICP-MS | 319 ± 2 | Zhang et al. (2015) |
| 12ZB56 | Zhibo iron deposit | Andesite | LA-ICP-MS | 328.7 ± 2.1 | Jiang et al. (2014b) |
| 12ZB06 | Zhibo iron deposit | Iron ore | LA-ICP-MS | 329.9 ± 1.5 | Jiang et al. (2014b) |
| IP028 | Beizhan iron deposit | Rhyolite | LA-ICP-MS | 316.1 ± 2.2 | Li et al. (2013) |
| YX8-1 | Yuximolegai | Quartz diorite | SIMS | 310.8 ± 2.1 | Yang et al. (2012) |
| 13WL | Wuling | Hornblende gabbro | LA-ICP-MS | 313 ± 3 | Yan et al. (2015) |
| 0837 | Qiaohuote copper deposit | Granodiorite | LA-ICP-MS | 450.4 ± 1.1 | Zhang et al. (2011) |
| 0844 | Qiaohuote copper deposit | K-feldspar granite | LA-ICP-MS | 430.8 ± 4.1 | Zhang et al. (2011) |
| CGB-2 | Chagangnuoer iron deposit | Basalt | LA-ICP-MS | 314 ± 8 | Li et al. (2015b) |
| 11QJ1-3 | Qunjisayi | Rhyolite | LA-ICP-MS | 306 ± 2 | Li et al. (2015c) |
| 10QJ-3D | Qunjisayi | Granite | LA-ICP-MS | 296 ± 3 | Li et al. (2015c) |
| TS17-1 | Xinyuan Forest Farm | Dacite | LA-ICP-MS | 359.9 ± 5.1 | Yu et al. (2016) |
| TS13-2 | Xinyuan Forest Farm | Monzogranite | LA-ICP-MS | 322.2 ± 2.9 | Yu et al. (2016) |
| 04XJ-263 | Southern Awulale | Syenite | SHRIMP | 311.9 ± 2.5 | Sun et al. (2008) |

## 3. Overview of the Awulale iron Metallogenic Belt

The AIMB is situated in the eastern part of the Yili-Central Tianshan Block and exposed as a linear belt along the Awulale Mountains (Fig. 1b). The AIMB, comprising-from west to east-the Kuolasayi, Shikebutai, Songhu, Nixintage-Akesayi, Chagangnuoer, Zhibo, Dunde and Beizhan iron ore deposits, is one of the most important iron ore provinces with high-grade ores in China (Fig. 1b; Zhang et al., 2014a). The iron deposits are generally hosted by submarine volcano-sedimentary sequences, which are part of the widespread early Carboniferous Dahalajunshan Formation (Zhang et al., 2014b). However, high-resolution geochronology documented that the Dahalajunshan Formation is a diachronous volcano-sedimentary sequence that formed during a time span of ca. 370–300 Ma (late Devonian to late Carboniferous) with ore-hosting rocks formed in a more restricted age range of ca. 330–300 Ma (middle to late Carboniferous; e.g., Zhang et al., 2012, 2015; Li et al., 2013, 2015b; Duan et al., 2014; Jiang et al., 2014b). The geochemical signatures of the volcanic rocks in the Dahalajunshan Formation suggested that they were generated in a continental arc setting (e.g., Zhu et al., 2005, 2009; Wang et al., 2007; Yu et al., 2016).

The ore-hosting volcanic rocks show a wide compositional variation including mafic, intermediate-mafic and intermediate-felsic rocks as well as their volcanoclastic equivalents. The iron ore mineralization hosted in lavas (i.e., Chaganguoer, Zhibo, Beizhan, Dunde, Songhu, Kuolasayi and Nixintage-Akesayi) generally forms stratiform, lenticular as well as vein-type ore bodies with magnetite as the dominant ore mineral. Extensively pervasive alteration includes common Ca, K and Na metasomatism (Zhang et al., 2014a,b). In addition, skarn-type alteration and mineralization is also developed at the contact zone between the orebodies and carbonates intercalated with volcanic rocks in some deposits, such as Chagangnuoer, Beizhan and Dunde. However, different from typical skarns, no plutons are present in these deposits (Zhang et al., 2014a,b). The iron ore mineralization that is hosted in pyroclastic-sedimentary rocks (i.e., Shikebutai) occurs as stratiform and

**Table 3**
Whole-rock Sr–Nd isotopic data of selected volcanic and intrusive rocks in the Awulale and adjacent areas.

| Sample | Rock type | Age (Ma) | Rb (ppm) | Sr (ppm) | $^{87}Rb/^{86}Sr$ | $^{87}Sr/^{86}Sr$ | $^{87}Sr/^{86}Sr(t)$ | Sm (ppm) | Nd (ppm) | $^{147}Sm/^{144}Nd$ | $^{143}Nd/^{144}Nd$ | $^{143}Nd/^{144}Nd(t)$ | $\varepsilon_{Nd}(t)$ | $T_{DM}$ (Ma) | $T_{2DM}$ (Ma) |
|---|---|---|---|---|---|---|---|---|---|---|---|---|---|---|---|
| 0838-1 | Basaltic andesite | 450[a] | 7.56 | 377 | 0.0581 | 0.70687 | 0.70650 | 5.55 | 21.0 | 0.15987 | 0.512802 | 0.512331 | 5.33 | 990 | 753 |
| 0839-1 | Basaltic andesite | 450 | 15.3 | 439 | 0.1008 | 0.70624 | 0.70559 | 5.70 | 20.7 | 0.16668 | 0.512826 | 0.512335 | 5.40 | 1056 | 747 |
| 0840-1 | Basaltic andesite | 450 | 7.82 | 439 | 0.0515 | 0.70664 | 0.70630 | 6.11 | 21.0 | 0.17619 | 0.512815 | 0.512296 | 4.64 | 1367 | 809 |
| 0840-2 | Basaltic andesite | 450 | 14.7 | 379 | 0.1121 | 0.70536 | 0.70464 | 5.70 | 21.0 | 0.16462 | 0.512828 | 0.512343 | 5.56 | 1005 | 734 |
| 0846-1 | Basalt | 450 | 10.3 | 259 | 0.1149 | 0.70626 | 0.70552 | 7.50 | 25.7 | 0.17633 | 0.512867 | 0.512347 | 5.64 | 1161 | 727 |
| 0846-8 | Basalt | 450 | 4.52 | 505 | 0.0259 | 0.70652 | 0.70635 | 4.72 | 16.6 | 0.17244 | 0.512845 | 0.512337 | 5.44 | 1133 | 744 |
| 0945-1 | Diorite | 306 | 105 | 275 | 1.111 | 0.70924 | 0.70440 | 3.96 | 17.2 | 0.13957 | 0.512770 | 0.512490 | 4.80 | 785 | 677 |
| 0945-2 | Diorite | 306 | 113 | 276 | 1.182 | 0.70959 | 0.70444 | 4.75 | 20.6 | 0.13962 | 0.512760 | 0.512480 | 4.61 | 806 | 693 |
| 0947-4 | Granite | 304[b] | 331 | 134 | 7.148 | 0.73349 | 0.70257 | 4.65 | 21.5 | 0.13128 | 0.512738 | 0.512477 | 4.50 | 765 | 701 |

[a] The age used for calculations of Silurian volcanic rocks is adopted from Xing et al. (2016).
[b] The age used for calculations is after Zhang et al. (2012).

lenticular lenses with haematite as the dominated ore mineral. Alteration in these deposits is mainly displayed by local chloritization, sericitization and carbonization (Zhang et al., 2014a). Based on correlation with the spatial-temporal evolution of the submarine volcanoes and principal volcanic facies variations, Hou et al. (2014) suggested that the iron ore mineralization in the lavas is relatively proximal to the volcanic vent while that in the pyroclastic-sedimentary rocks is more distal to the vent.

Numerous studies were undertaken to obtain the mineralization ages and to gain insight into the metallogenesis of the submarine volcanic-hosted iron deposits of the AIMB. For example, Duan et al. (2014) obtained a zircon U–Pb age of 316.0 ± 1.7 Ma for an ore-bearing dacite in the Dunde iron deposit. A rhyolite in the Beizhan iron deposit yielded a zircon U–Pb age of 316.1 ± 2.2 Ma, which was also interpreted as the age of the iron mineralization (Li et al., 2013). Based on the zircon U–Pb ages of the ore-hosting volcanic rocks the Zhibo and Changangnuoer iron deposits were thought to occur at ca. 330–316 Ma (Zhang et al., 2012, 2015; Jiang et al., 2014b) and ca. 321–319 Ma (Li et al., 2015b; Zhang et al., 2015), respectively. This is supported by the skarn-type alteration assemblages of garnet-actinolite-epidote yielding two Sm–Nd isochron ages of 316.8 ± 6.7 and 313 ± 7 Ma at the Chagangnuoer deposit (Hong et al., 2012; Zhang et al., 2015).

The AIMB iron ore deposits exhibit many geological, mineralogical and geochemical similarities with other alkali-calcic, hydrothermal altered volcanic-hosted iron ore deposits, which are the subject of a long-standing, controversial discussion concerning a possible magmatic or hydrothermal origin, or a combination of both (e.g., Henriquez and Martin, 1978; Nystroem and Henriquez, 1994; Nystroem et al., 2008; Wang et al., 2011b; Hong et al., 2012; Dare et al., 2014; Jiang et al., 2014b; Zhang et al., 2012, 2015; Tornos et al., 2016; Günther et al., 2017). This was recently explored by a combined O- and Fe-isotope study of the primary ore mineral magnetite at Zhibo and Chagangnuoer which favored an orthomagmatic origin for most of the massive ore and a hydrothermal origin for the re-precipitated skarn-type iron ore (Günther et al., 2017). However, the poorly constrained origin of the iron mineralization is beyond the scope of this paper and we will focus on the discussion of the tectonic setting of the submarine volcanic-hosted iron ore deposits in the AIMB.

## 4. Results

Field work was conducted in the eastern part of the Chinese Western Tianshan and forty-eight samples were collected from intrusive and volcanic rocks in the AIMB and adjacent areas. Eleven samples of Paleozoic intrusions were selected for LA-ICP-MS zircon U–Pb dating at the State Key Laboratory of Geological Processes & Mineral Resources of the China University of Geosciences (Beijing). The other thirty-seven samples were analyzed for whole-rock major and trace elements and nine of them for whole-rock Sr–Nd isotopes at the Institute of Geology and Geophysics, Chinese Academy of Sciences (IGGCAS). Descriptions of the studied igneous rocks, including rock types, sampling sites and coordinates, mineral assemblages and magmatic ages are summarized in Tables 1 and 2. Furthermore, the locations of the dated samples are shown in Figs. 1b and 2. The analytical data of zircon U–Pb geochronology and whole-rock geochemistry are listed in Supplementary Tables S1 and S2, respectively. The whole-rock Sr–Nd isotopic data are presented in Table 3. The detailed analytical techniques are summarized in Supplementary Appendix A.

### 4.1. Zircon U–Pb ages

Zircon grains from the eleven granitoid samples are generally euhedral, prismatic or equant in morphologies. Under cathodoluminescence (CL) images, they are characterized by homogeneous or well-developed compositional zoning patterns, such as oscillatory zoning, sector zoning and broad-stripped zoning (insets in Fig. 4), all of which

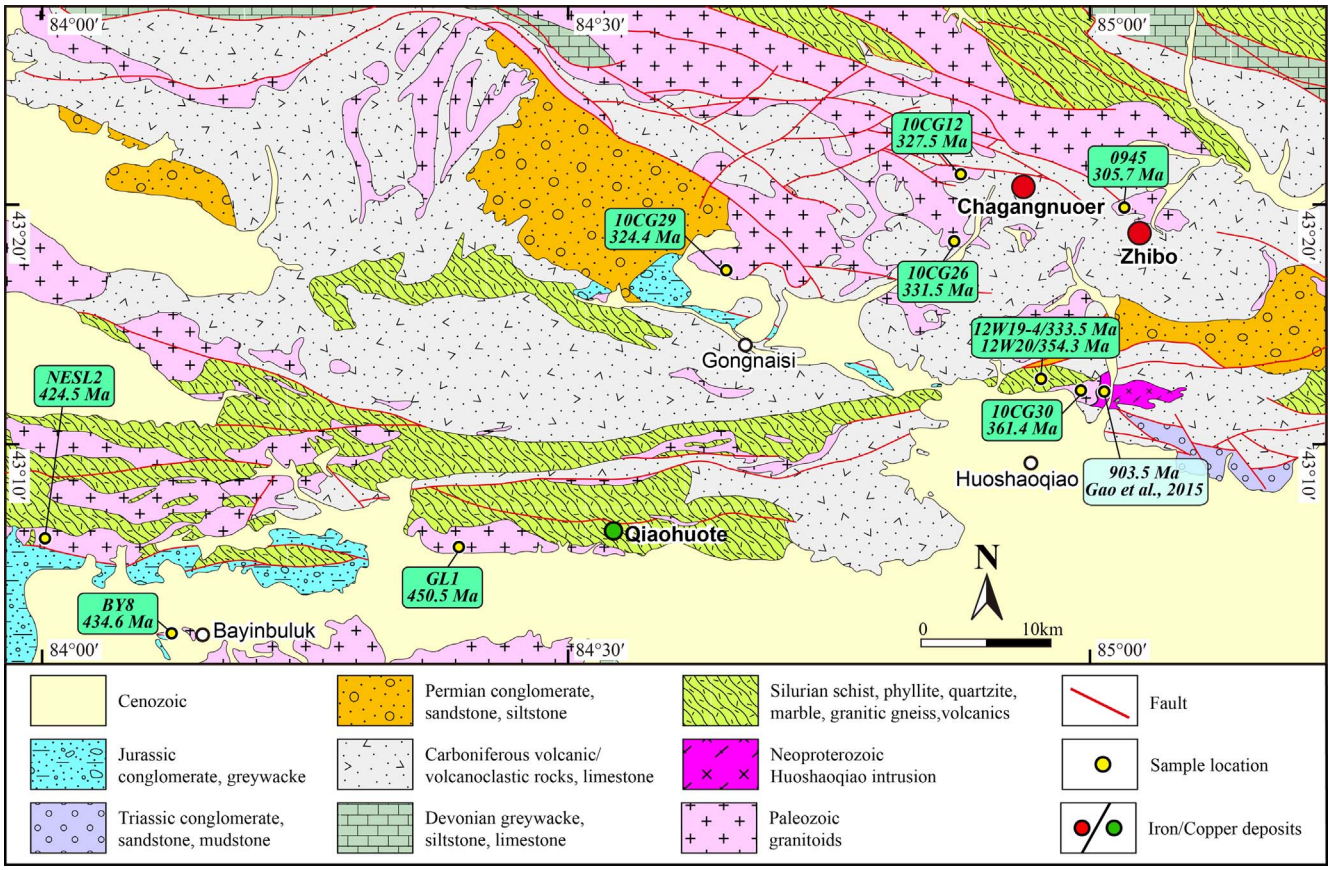


**Fig. 2.** Geological map of the eastern segment of the Awulale Iron Metallogenic Belt in Chinese Western Tianshan (Modified after 1:200,000 geological maps by XBGMR (1972a,b)). Note that locations of Paleozoic igneous rocks with zircon U–Pb ages in this study are denoted. The Neoproterozoic Huoshaoqiao intrusion in the periphery of the Zhibo iron deposit is also marked with its emplacement age (Gao et al., 2015).

are typical of magmatic zircon grains (Corfu et al., 2003). All zircon analyses show variable Th (37.1–1124 ppm) and U (68.7–1517 ppm) contents with scattered Th/U ratios of 0.26–2.71 (Table S1). A total of 238 analyzed zircon grains from the eleven individual rock samples produced relatively uniform $^{206}Pb/^{238}U$ ages within a 95–108% concordancy with respect to their $^{207}Pb/^{235}U$ ages (Table S1). Accordingly, in the concordia diagrams, concordia ages of 450.5 ± 1.5 Ma (MSWD = 0.008, n = 18), 441.5 ± 1.1 Ma (MSWD = 1.5, n = 24), 434.6 ± 3.6 Ma (MSWD = 3.4, n = 16), 424.5 ± 1.4 Ma (MSWD = 0.019, n = 17), 361.4 ± 0.94 Ma (MSWD = 0.065, n = 27), 354.3 ± 1.7 Ma (MSWD = 7.2, n = 16), 333.5 ± 2.1 Ma (MSWD = 0.48, n = 17), 331.5 ± 0.91 Ma (MSWD = 13, n = 25), 327.5 ± 0.86 Ma (MSWD = 0.34, n = 27), 324.4 ± 0.88 Ma (MSWD = 0.83, n = 29) and 305.7 ± 0.88 Ma (MSWD = 0.007, n = 21) for samples GL1, JT17, BY8, NESL2, 10CG30, 12W20, 12W19-4, 10CG26, 10CG12, 10CG29 and 0945, respectively (Fig. 4). Therefore, these ages are interpreted as the respective crystallization ages of the granitoids.

### 4.2. Geochemical characteristics

Our 37 new whole-rock major and trace element geochemical analyses were combined with published data for 312 Paleozoic igneous rocks in the AIMB and adjacent areas compiled from the literature (Tables 2 and S3). The zircon U–Pb ages for 52 Paleozoic igneous rocks suggest that a protracted magmatism (450–290 Ma) was present in the eastern part of the Yili-Central Tianshan Block (Table 2). As noted above, the (U)HP metamorphism of the Akeyazi high-pressure metamorphic terrane occurred in a restricted period of ca. 320–310 Ma and it was employed to place constraints on the timing of the collision between the Yili-Central Tianshan Block and the Tarim Craton (e.g., Su et al., 2010; Yang et al., 2013), which may indicate that a distinct tectonic process took place in the specific time window. In this regard, these igneous rocks are divided into three groups based on the short-lived subduction-zone peak metamorphism: 450–321 Ma, predating the peak metamorphism; 320–310 Ma, coeval with the peak metamorphism; 309–290 Ma, postdating the peak metamorphism (see explanation in Section 5.2).

The 450–321 Ma and 320–310 Ma igneous rocks exhibit a similar compositional range from basalt (gabbro) to rhyolite (granite) in the TAS diagram, while most of the 309–290 Ma magmatic rocks plot in the rhyolite field except the diorites of this study (Fig. 5a). With respect to the $K_2O$ contents, the 450–321 Ma igneous rocks are mainly medium- and high-K calc-alkaline with a few being low-K tholeiitic or shoshonitic (Fig. 5b). In contrast, the 320–310 Ma igneous rocks are mostly medium-K, high-K calc-alkaline and shoshonitic rocks. The 309–290 Ma magmatic rocks are predominately high-K calc-akaline (Fig. 5b). The granitic rocks ($SiO_2$ > 56 wt%) of these three groups generally range in composition from calcic to alkalic and are mostly metaluminous to weakly peraluminous with A/CNK ratios of 0.6–1.2 (Fig. 8c and d). In the binary diagrams, MgO, CaO and $Fe_2O_3T$ contents of the igneous rocks from the three groups display strongly negative correlations with $SiO_2$ contents (Fig. 6). However, $Al_2O_3$, $TiO_2$, $P_2O_5$, Zr are characterized by an initially weak positive trend followed by a strong negative trend as the rocks evolved (Fig. 6). Notably, Sr contents are generally lower than 500 ppm without obvious correlations as $SiO_2$ increases (Fig. 6h).

All magmatic rocks exhibit broadly similar chondrite-normalized rare earth element (REE) patterns despite their variable total REE contents (Fig. 7). Collectively, they are characterized by weak to strong enrichment of LREE relative to HREE with notably steep LREE and flat

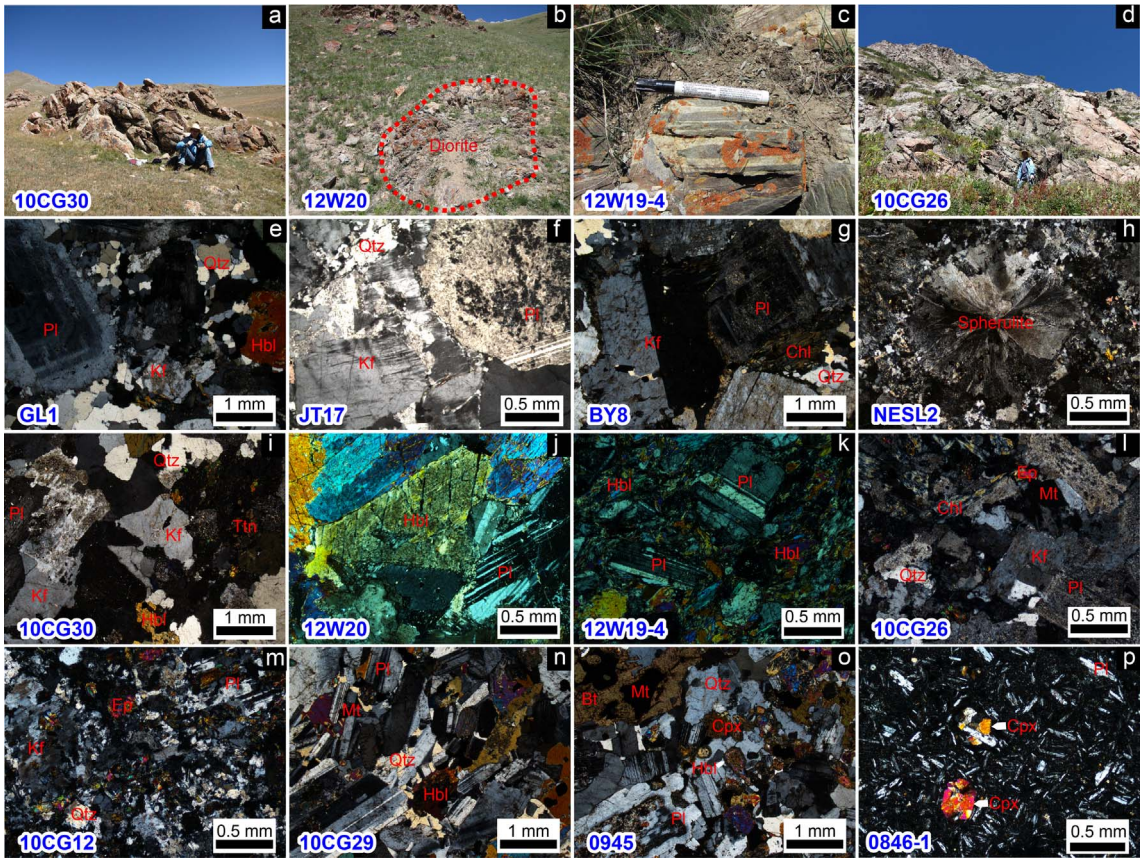


**Fig. 3.** Representative photomicrographs showing textures and mineral associations of the Paleozoic igneous rocks in the Awulale and adjacent areas, as well as some field photos showing outcrops. Abbreviations: Pl-plagioclase, Kf-K-feldspar, Qtz-quartz, Ttn-titanite, Hbl-hornblende, Chl-chlorite, Mt-magnetite, Ep-epidote, Bt-biotite, Cpx-clinopyroxene.

HREE patterns (Fig. 7). Weak to pronounced negative Eu anomalies ($Eu/Eu^*$) are commonly present in most rocks, suggesting significant plagioclase fractionation during magmatic differentiation (Figs. 6g and 7). Similarly, the primitive mantle-normalized trace element patterns are similar for all igneous rocks, including the enrichment of large-ion lithophile elements (LILEs: Rb, Ba, Th, U, K) compared to high-field strength elements (HFSEs) and remarkable Nb, Ta and Ti troughs (Fig. 7).

### 4.3. Whole-rock Sr–Nd isotopes

In this study, six samples from the Silurian volcanic rocks in the Qiaohuote copper deposit, two samples from the ca. 306 Ma diorite (0945) and one sample from the 304 Ma granite (0947; Zhang et al., 2012) were selected for whole-rock Sr–Nd isotopic analyses (Table 3). The Silurian volcanic rocks are mainly composed of basalts, basaltic andesites and andesites (Fig. 3p), which have been subjected to regional greenschist-facies metamorphism. Recently, the formation ages of basaltic andesites and dacites from the Silurian volcanic rocks in the Bayinbuluke area were constrained between 455.6 ± 8.1 and 444.5 ± 1.9 Ma by LA-ICP-MS zircon U–Pb dating, indicating a late Ordovician eruption (Xing et al., 2016). Thus, we calculated the initial Sr–Nd isotopic compositions of the Silurian volcanic rocks using an age of ca. 450 Ma. These rocks show relatively restricted initial $^{87}Sr/^{86}Sr$ ratios of 0.70464–0.70650 and positive $\varepsilon_{Nd}(t)$ values of +4.64 to +5.64 (Table 3). Similarly, the 305.7 ± 0.9 Ma diorite (0945) and the 304.1 ± 1.8 Ma granite (0947) yielded relatively low initial $^{87}Sr/^{86}Sr$ ratios of 0.70257–0.70444 and positive $\varepsilon_{Nd}(t)$ values of +4.50 to +4.80 (Table 3).

In combination with published Nd isotopic compositions for 114 Paleozoic igneous rocks in the Awulale and adjacent areas (Table S3), the three groups of igneous rocks as defined above display different $\varepsilon_{Nd}(t)$ values. Overall, the 450–321 Ma igneous rocks exhibit scattered $\varepsilon_{Nd}(t)$ values from −3 to +7 and have no clear correlations with the $SiO_2$ contents (Fig. 9c and d). In contrast, the 320–310 Ma and 309–290 Ma magmatic rocks are characterized by more restricted $\varepsilon_{Nd}(t)$ values ranging from +2 to +6 with the exception of one negative value. Notably, despite the highly variable $SiO_2$ contents, no obvious trends are observed in the $\varepsilon_{Nd}(t)$ values of the two groups (Fig. 9c and d). In addition, as shown in Fig. 9c, the $\varepsilon_{Nd}(t)$ values of the igneous rocks increase gradually as their formation ages decrease.

## 5. Discussion

### 5.1. Petrogenesis of the Paleozoic igneous rocks

In conjunction with data from the literature our geochronological and geochemical study reveals that the prolonged Paleozoic magmatism in the AIMB and adjacent areas share common geochemical signatures. In terms of major elements, they exhibit a continuous spectrum extending from basalts (gabbros) to high-silica rhyolites (granites). However, it should be noted that these Paleozoic igneous rocks were formed in a wide age range with distinct whole-rock $\varepsilon_{Nd}(t)$ values, which suggests that they cannot be produced from a common magma source. Compared to the compiled geochemical dataset of continental igneous rocks globally (See Figs. 1 and 2 in Keller et al., 2015), the Paleozoic igneous rocks in the AIMB have broadly similar abundances of major and trace elements. Interestingly, some igneous rocks from the 450–321 and 320–310 Ma groups show increased $Fe_2O_3T$ and $TiO_2$ contents at a given silica content, which resembles the tholeiitic characters of mid-ocean ridge basalts and rift volcanic rocks in continental crust. Since the strong correlation has been well stablished between

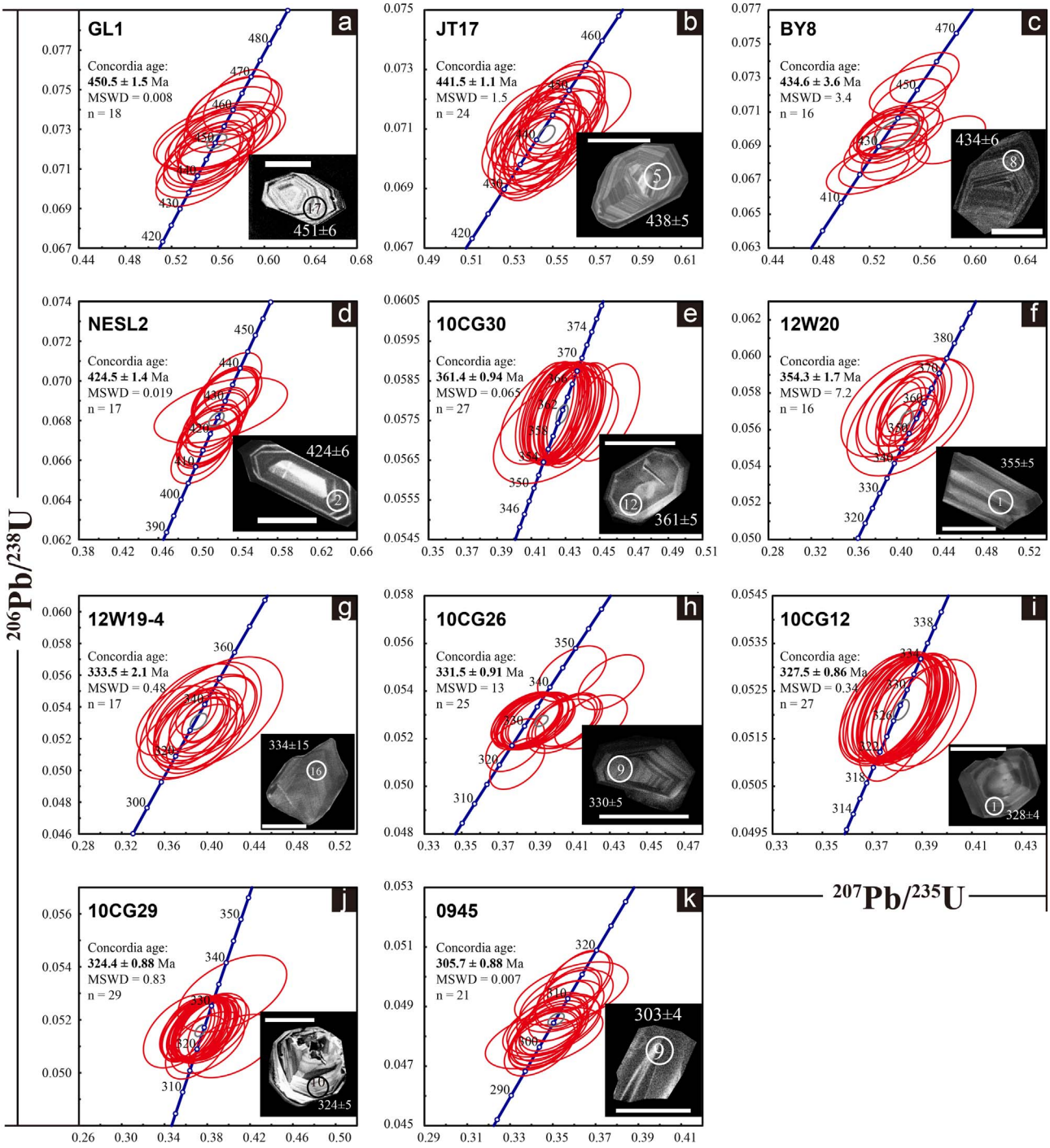


**Fig. 4.** LA-ICP-MS zircon U–Pb Concordia diagrams for the Paleozoic igneous rocks in the Awulale and adjacent areas of the Chinese Western Tianshan. The insets are selected CL images of zircon grains showing zoning patterns of typical magmatic origin. The white scale bars are 100 μm long.

water content and the degree of tholeiitic versus calc-alkaline magmatic trends (Sisson and Grove, 1993; Zimmer et al., 2010; Keller et al., 2015), this observation is consistent with a slightly anhydrous composition for these igneous rocks. In general, dissolved water in the silicate melts could lower the liquidus and solidus temperatures so that most silicate minerals become saturated in the magma at lower temperatures, with a particularly strong influence for sodic plagioclase (Green and Ringwood, 1968; Sisson and Grove, 1993). Therefore, it is expected that the negative Eu/Eu* and decreased Sr contents in the Paleozoic igneous rocks are attributed to enhanced plagioclase fractionation during anhydrous differentiation. In addition, given the suppressed zircon and apatite solubility under dry and hot crystallization, Zr and P contents in the magmas will peak at higher silica contents than under wet and cooler crystallization (e.g., Lee and Bachmann, 2014). As shown in Fig. 6f and i, the Paleozoic igneous rocks in the AIMB are characterized by elevated $P_2O_5$ and Zr contents at a given silica content, which consistently plot closer to the modeled liquid lines of descent under anhydrous and low-pressure conditions. Consequently, it is reasonable to infer that the Paleozoic igneous rocks in the AIMB are formed by crystal fractionation of their respective parental magmas under relatively dry and low-pressure conditions. However, equilibrium melting and equilibrium crystallization are generally indistinguishable with respect to geochemistry (Lee and Bachmann, 2014) and, thus, partial melting of pre-existing mafic rocks cannot be excluded to

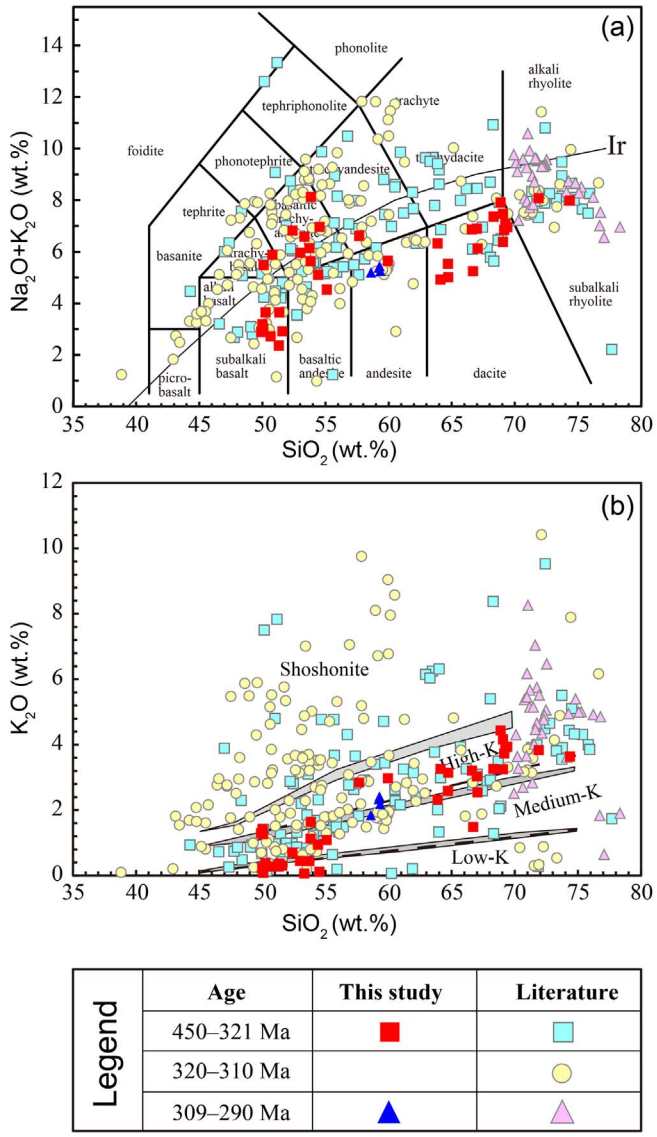


**Fig. 5.** (a) Total alkali-silica diagram (Le Bas et al., 1986) and (b) $K_2O$–$SiO_2$ plot (Peccerillo and Taylor, 1976) showing compositional variations of the Paleozoic (ca. 450–290 Ma) igneous rocks in the Awulale and adjacent areas based on compilation of published and new data (data sources see Table S3). Note that the igneous rocks are subdivided into three groups based on peak metamorphism (ca. 320–310 Ma) of the Akeyazi high-pressure metamorphic terrane (see text for explanation).

generate some silicic rocks, which is likely the case for the origin of the 309–290 Ma high-silica rocks.

In terms of trace elements, nearly all Paleozoic magmatic rocks are characterized by enrichments of LREEs and LILEs, depletions of HREEs and HFSEs as well as notable negative anomalies for Nb, Ta and Ti (Fig. 7), which are typical for subduction-related igneous rocks. As already noted above, such patterns reflect geochemical signatures of their source compositions, suggesting that they may be produced in a subduction setting or derived from partial melting of magmatic sources with arc signatures in a non-subduction setting (Fiannacca et al., 2015). Furthermore, the uniformly flat HREE patterns (Fig. 7) indicate that garnet was never involved in the origin of the Paleozoic igneous rocks and hence they may have formed at relatively low pressures (< 1 GPa; e.g., Rapp and Watson, 1995; Xiong et al., 2005; Lee et al., 2007; Richards et al., 2017).

In addition, the contrasting whole-rock $\varepsilon_{Nd}(t)$ for the three groups of Paleozoic igneous rocks seem to be consistent with different magma sources or variable amounts of crustal contamination during their generation. However, the wide whole-rock $\varepsilon_{Nd}(t)$ range of the broadly synchronous igneous rocks and the absence of a good correlation between $\varepsilon_{Nd}(t)$ and $SiO_2$ (Fig. 9) suggests that negligible crustal contamination occurred during late magmatic differentiation process at crustal levels. Therefore, the highly variable $\varepsilon_{Nd}(t)$ for the 450–321 Ma igneous rocks requires enriched/depleted mantle and ancient/juvenile pre-existing crust components with various degrees of mixing involved in the genesis of their parental magmas. In contrast, the more radiogenic and relatively constant $\varepsilon_{Nd}(t)$ values for the 320–310 Ma and 309–290 Ma magmatic rocks over scattered $SiO_2$ contents suggest that the magmatic differentiation trend resulted from crystal-liquid segregation in a closed system (Lee and Bachmann, 2014; Lee and Morton, 2015), or alternatively from mixing of isotopically similar depleted mantle and juvenile pre-existing crust components in an open system (Lee et al., 2007).

To further constrain the petrogenesis of the Paleozoic igneous rocks, major and trace element values are employed to explore source characteristics and formation conditions of the mafic ($SiO_2$ < 53 wt%) and granitic ($SiO_2$ > 56 wt%) rocks, respectively. In general, the mafic igneous rocks with low $SiO_2$ contents are thought to be products of mantle-derived magmas through magmatic differentiation. They are characterized by relatively restricted La/Yb ratios irrespective of variable Yb contents (Fig. 8a), suggesting that their parental magmas are mainly derived from high-degree partial melting of mantle sources in the spinel stability field (Miller et al., 1999). In addition, most mafic rocks exhibit high-K calc-alkaline and shoshonitic signatures and thus indicate a K-bearing phase, such as amphibole or phlogopite in their mantle sources. Variably elevated Rb/Sr ratios and relatively low Ba/Rb ratios (Fig. 8b) is consistent with phlogopite as the dominant mineral phase in their source regions (Furman and Graham, 1999). Furthermore, they display scattered Nb/Yb and relatively high Th/Yb ratios, indicating that their mantle sources have been modified by ongoing or previous subduction-related metasomatism (Pearce, 2014). In conclusion, we propose that the Paleozoic mafic rocks in the Awulale and adjacent areas were formed by relatively high-degree melting of metasomatized phlogopite-bearing mantle sources in the spinel stability field.

The granitic ($SiO_2$ > 56 wt%) rocks exhibit uniformly low Sr/Y ratios and thus plot within the field of typical arc rocks with few exceptions (Castillo et al., 1999; Richards and Kerrich, 2007; Fig. 8e). Along with the flat HREE and HFSE patterns, they do not display a significant garnet trace-element signature, which indicates an origin by a relatively thin differentiation column in a thinning continental crust (Lee et al., 2007; Chiaradia, 2015; Richards et al., 2017). In addition, the granitic rocks with metaluminous to weakly peraluminous signatures (Fig. 8d) display a marked $P_2O_5$ decline due to apatite fractionation (Fig. 6f), which is in contrast with positive trends in strongly peraluminous magmas (Wolf and London, 1994). Moreover, most of the granitic rocks show relatively low 10,000 * Ga/Al (< 3) ratios and Nb contents (< 30 ppm), which are distinct from the typical A-type granites and thus are belonging to I-type and highly fractionated I-type granites (Fig. 8f; Chappell and White, 1992; Whalen et al., 1987). However, it is noteworthy that some of the granitic rocks exhibit similar geochemical affinities to typical A-type granites (Zhang et al., 2012; Li et al., 2015c; Zhong et al., 2017). In general, typical A-type granites are thought to be generated in thin continental crusts associated with an extensional setting (Whalen et al., 1987; Patiño Douce, 1999). As discussed above, crystal fractionation or partial melting under relatively dry conditions and low pressures could be responsible for the geochemical affinities of A-type granites. In summary, we propose that the Paleozoic granitic rocks in the Awulale and adjacent areas were derived from crystal fractionation or partial melting in a thin continental crust due to extension.

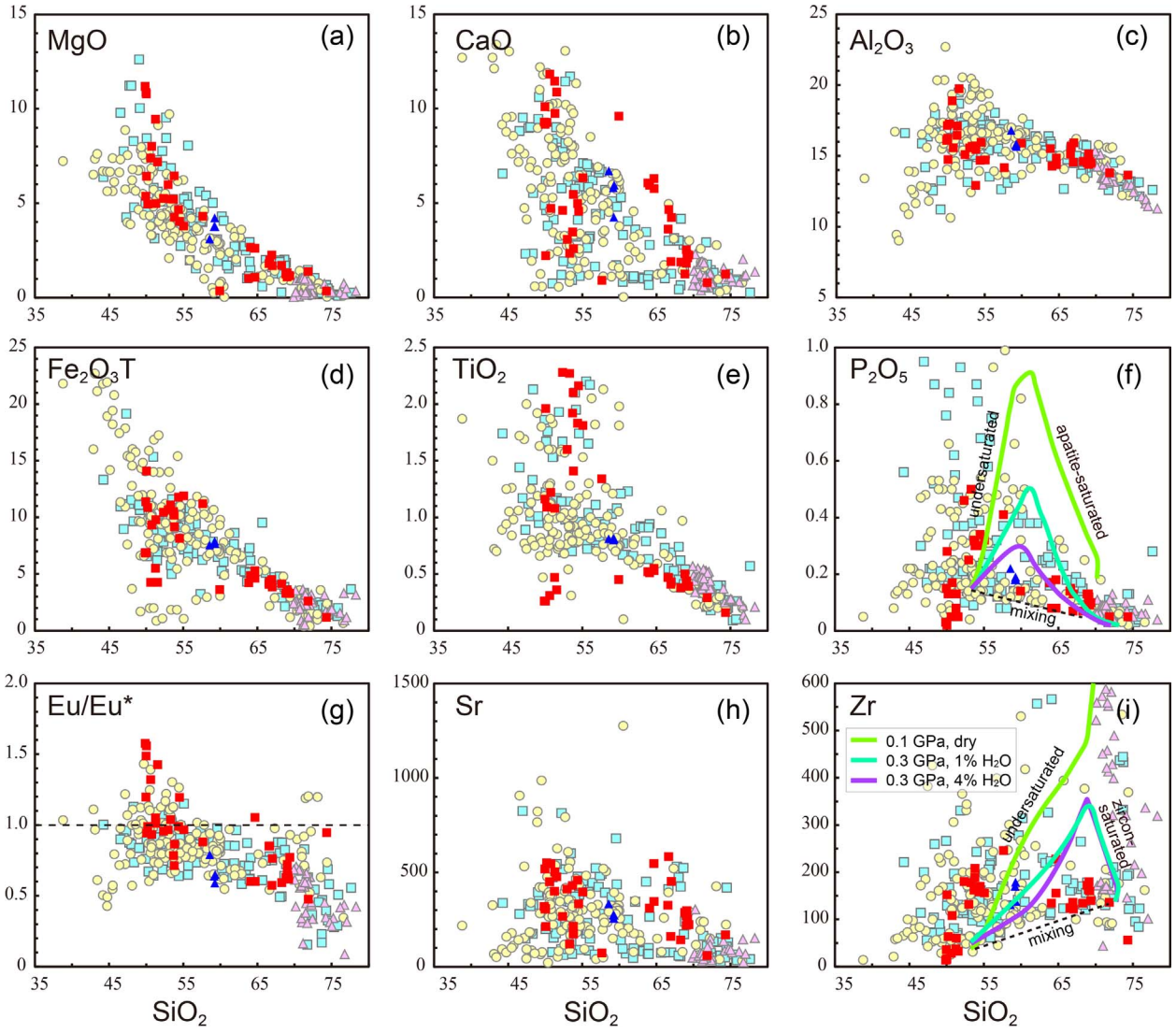


**Fig. 6.** Plots of whole-rock major (wt%) and trace (ppm) elements versus $SiO_2$ (wt%) for the Paleozoic magmatic rocks in the Awulale and adjacent areas. Note that colored curve lines represent modeled liquid lines of decent formed by equilibrium crystallization of dry and hydrous parental basalts, and straight dashed line is hypothetical mixing line between low silica and high silica endmembers (Lee and Bachmann, 2014) in (f) and (i). Symbols as in Fig. 5. (For interpretation of the references to colour in this figure legend, the reader is referred to the web version of this article.)

### *5.2. A slab-breakoff model for submarine volcanic-hosted iron mineralization*

Before discussing the exact tectonic setting of the submarine volcanic-hosted iron ore deposits in the Chinese Western Tianshan, the controversy of the Paleozoic tectonic evolution of the South Tianshan needs to be addressed. Since all the Paleozoic magmatic rocks in the Awulale and adjacent areas have similar arc geochemical signatures, a reconstruction of the tectonic setting during their formation cannot be solely based on the source-inherited characteristics. Therefore, the subduction-zone peak metamorphism and the exhumation of the Akeyazi high-pressure metamorphic terrane are employed to reconstruct the tectonic evolution of the South Tianshan.

The Akeyazi high-pressure metamorphic terrane is exposed as a Paleozoic metamorphosed accretionary complex along the South Central Tianshan Suture Zone (Fig. 1b) and its formation is thought to have resulted from the final closure of the South Tianshan Ocean and subsequent collision between the Yili-Central Tianshan Block and the Tarim Craton (Gao and Klemd, 2003; Su et al., 2010; Gao et al., 2011; Li et al., 2016). Numerous studies on the (U)HP rocks (i.e., eclogites, blueschists) concerning the timing of the peak metamorphism give a relatively restricted well-defined age range of 320–310 Ma (Fig. 9b) involving different high-resolution dating methods, such as SIMS/SHRIMP U–Pb dating of zircon (Su et al., 2010; Yang et al., 2013; Liu et al., 2014; Tan et al., 2017) and rutile (Li et al., 2011), whole-rock–mineral isochrons of Lu–Hf (Klemd et al., 2011) as well as Rb–Sr (John et al., 2012; van der Straaten et al., 2012) and Sm–Nd (Du et al., 2014; Soldner et al., 2017) isotopic systematics. The subsequent exhumation of the (U)HP rocks is believed to have occurred through a 'sediment-type subduction channel' model (Li et al., 2016) in a relatively short time frame of ca. 310–300 Ma as evidenced by white mica Ar–Ar and Rb–Sr ages (Klemd et al., 2005) and recrystallized zircon U–Pb ages (Tan et al., 2017).

Notably, a distinct magmatic flare-up between ca. 320 and 310 Ma, which is coeval with the peak metamorphism, was recognized in the Awulale and adjacent areas (Fig. 9a; Table 2). The 320–310 Ma igneous rocks are characterized by relatively constant and highly positive $\varepsilon_{Nd}(t)$ over a wide range of $SiO_2$, indicating a dominant contribution of depleted mantle component. Thus, we propose that the synchronicity of intensive magmatism and subsequently rapid exhumation of (U)HP rocks is the consequence of slab breakoff. Numerical stimulations documented that slab breakoff could take place when the slab-pull of

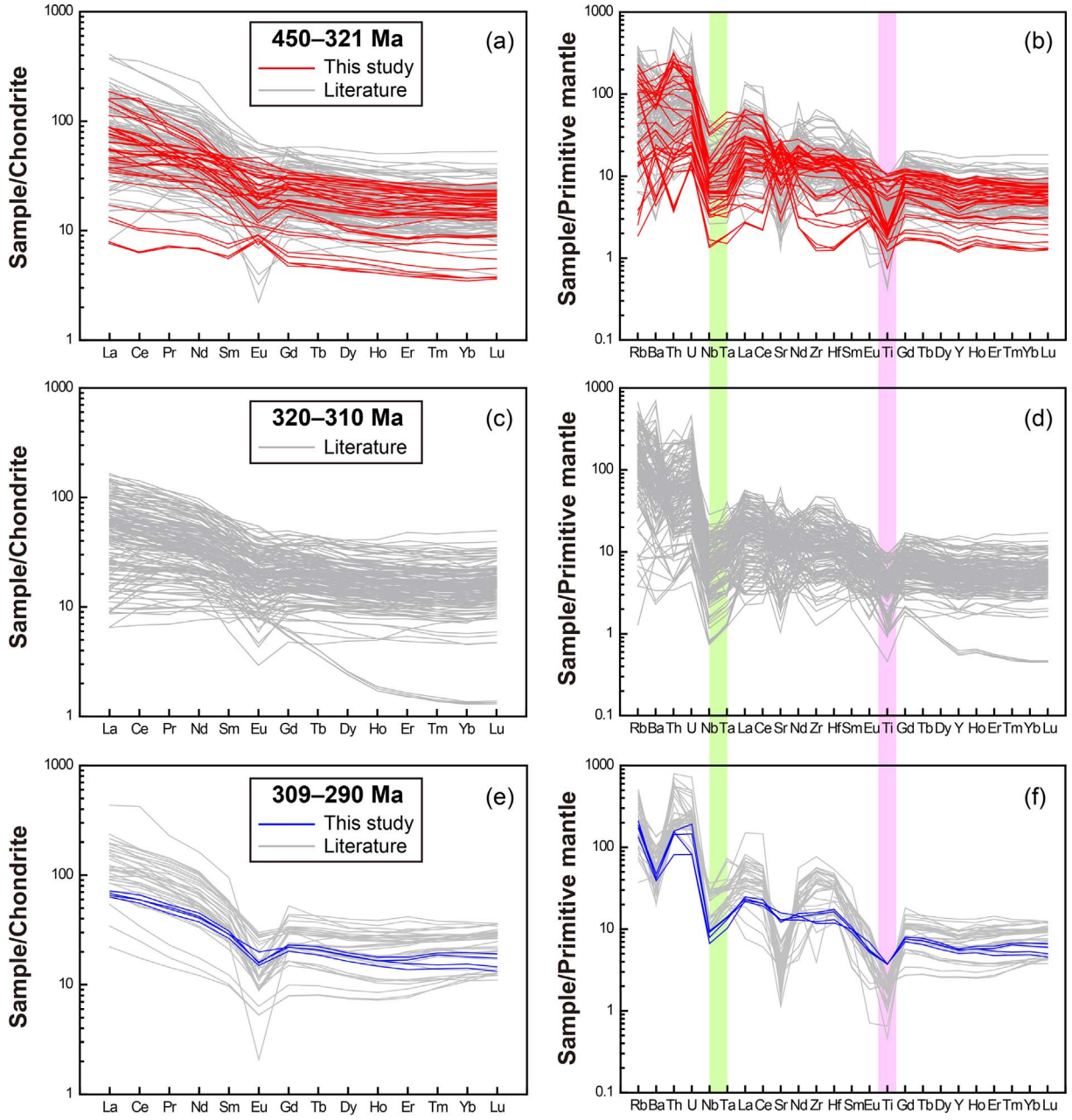


**Fig. 7.** Chondrite-normalized REE patterns and primitive mantle-normalized trace element diagrams for the three groups of Paleozoic igneous rocks in the Awulale and adjacent areas in Chinese Western Tianshan. Normalized values are from Sun and McDonough (1989). The geochemical data are compiled in Table S3.

the subducted oceanic lithosphere exceeds the positive buoyancy of the attached continental lithosphere (Davies and von Blanckenburg, 1995; Warren, 2013). As a result, the upwelling of asthenospheric mantle through slab window will trigger partial melting by decompression of asthenosphere and heating of the overlying mantle wedge (Davies and von Blanckenburg, 1995; Zhu et al., 2015), thus producing intensive magmatism with depleted Nd isotopic compositions in this study. Meanwhile, the rebounding of the positively buoyant relic slab will be conducive to the rapid exhumation of (U)HP rocks as well as facilitated by the extensional regime in response to asthenospheric upwelling (Davies and von Blanckenburg, 1995; Warren et al., 2008; Hacker and Gerya, 2013). The short-lived exhumation of oceanic (U)HP rocks in the southwestern Tianshan is interpreted to take place towards the end of oceanic subduction (Gao et al., 2011; Li et al., 2016; Tan et al., 2017), which is likely the case for Western Alps and New Caledonia (Agard et al., 2009). Therefore, slab breakoff at ca. 320–310 Ma enables us to place constraints on the tectonic evolution of the South Tianshan.

In general, slab breakoff is thought to be inevitable subsequent to the termination of oceanic subduction and the initiation of continental collision (e.g., Davies and von Blanckenburg, 1995; van Hunen and Allen, 2011; Zhu et al., 2015). It is suggested that slab breakoff provides a lower limit for the timing of continental collision and, hence, the initial collision between the Yili-Central Tianshan Block and the Tarim Craton probably commenced slightly earlier than ca. 320–310 Ma. Thus, we interpret the 450–321 Ma igneous rocks in the Awulale and adjacent areas as a product of the continental arc magmatism during northward-subduction of the South Tianshan Ocean. This interpretation is further supported by 439–332 Ma ophiolites in the South Central Tianshan Suture Zone (Jiang et al., 2014a) and ca. 400 Ma high-temperature metamorphism and anataxis in the migmatite complex juxtaposed against the Akeyazi terrane, which constituents a paired metamorphic belt (Xia et al., 2014). Notably, the 450–321 Ma igneous rocks

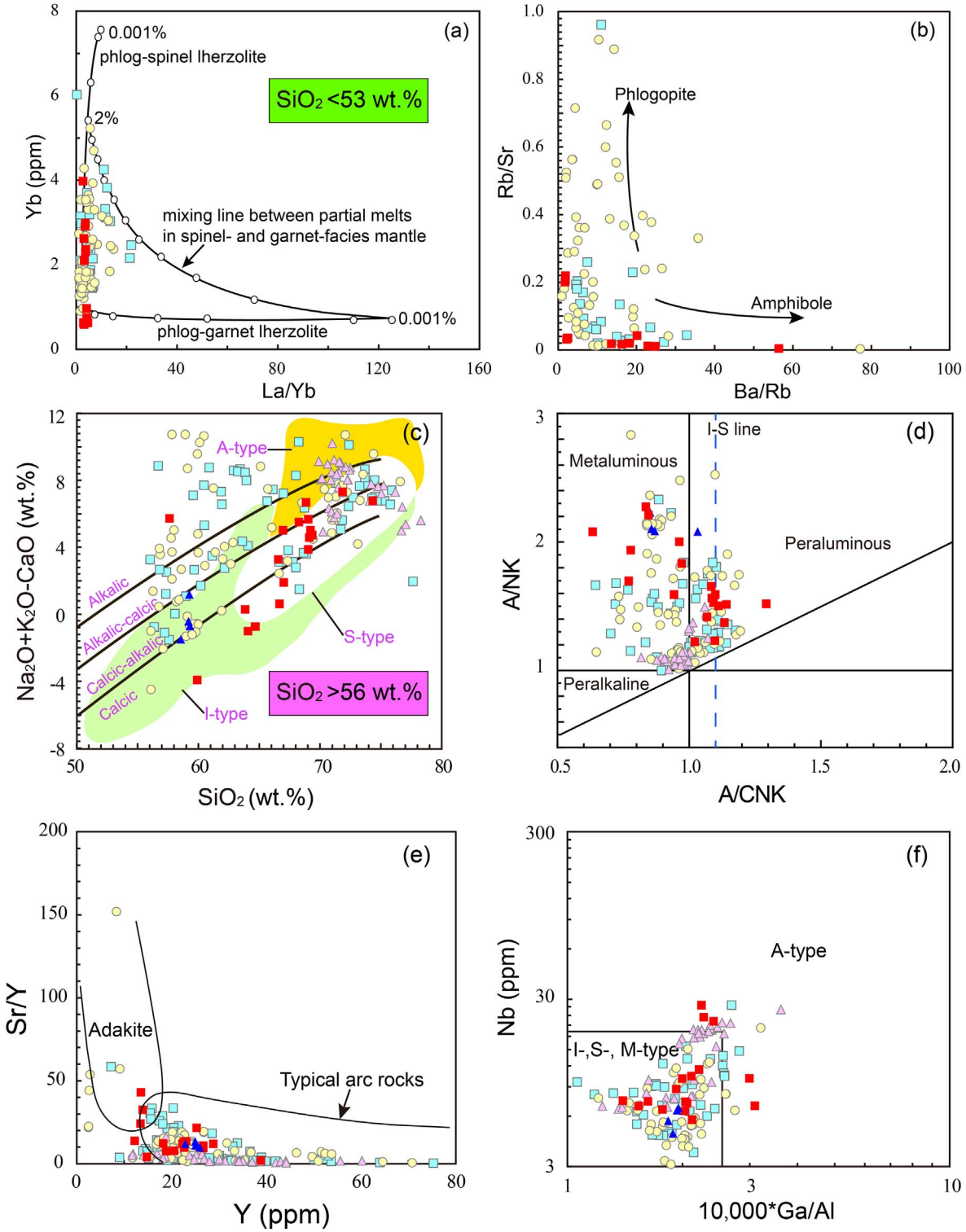


**Fig. 8.** Diagrams of (a) La/Yb–Yb showing the Paleozoic mafic rocks ($SiO_2$ < 53 wt%) in the Awulale and adjacent areas derived from partial melting of mantle sources in the spinel stability field (Miller et al., 1999) and (b) Ba/Rb–Rb/Sr indicating phlogopite as the dominated mineral phase in their source regions (Furman and Graham, 1999). (c–f) Discrimination diagrams for the Paleozoic granitic ($SiO_2$ > 56 wt%) rocks in the Awulale and adjacent areas: (c) $Na_2O + K_2O$-CaO–$SiO_2$ plot (Frost et al., 2001); (d) A/CNK–A/NK plot (Maniar and Piccoli, 1989); (e) Sr/Y–Y plot (Castillo et al., 1999; Richards and Kerrich, 2007); (f) Nb–10,000 * Ga/Al plot (Whalen et al., 1987). Symbols as in Fig. 5.

record a long-term shift towards increasingly positive $\varepsilon_{Nd}(t)$ values (Fig. 9c). This implies increasing additions of juvenile materials derived largely from the underlying convective mantle wedge, which is typical of retreating accretionary orogens (Collins et al., 2011). In retreating orogens, removal of ancient lower crust and subcontinental lithospheric mantle and coeval crustal thinning will be triggered by continuously subduction-induced mantle flow (Currie et al., 2008; Collins et al., 2011), which is consistent with the generation of the 450–321 Ma igneous rocks at relatively low pressures as discussed above. Thus, we propose that slab rollback/retreating is more likely to account for the distinctively geochemical signatures of the 450–321 Ma arc magmatism during the northward-subduction of the South Tianshan Ocean

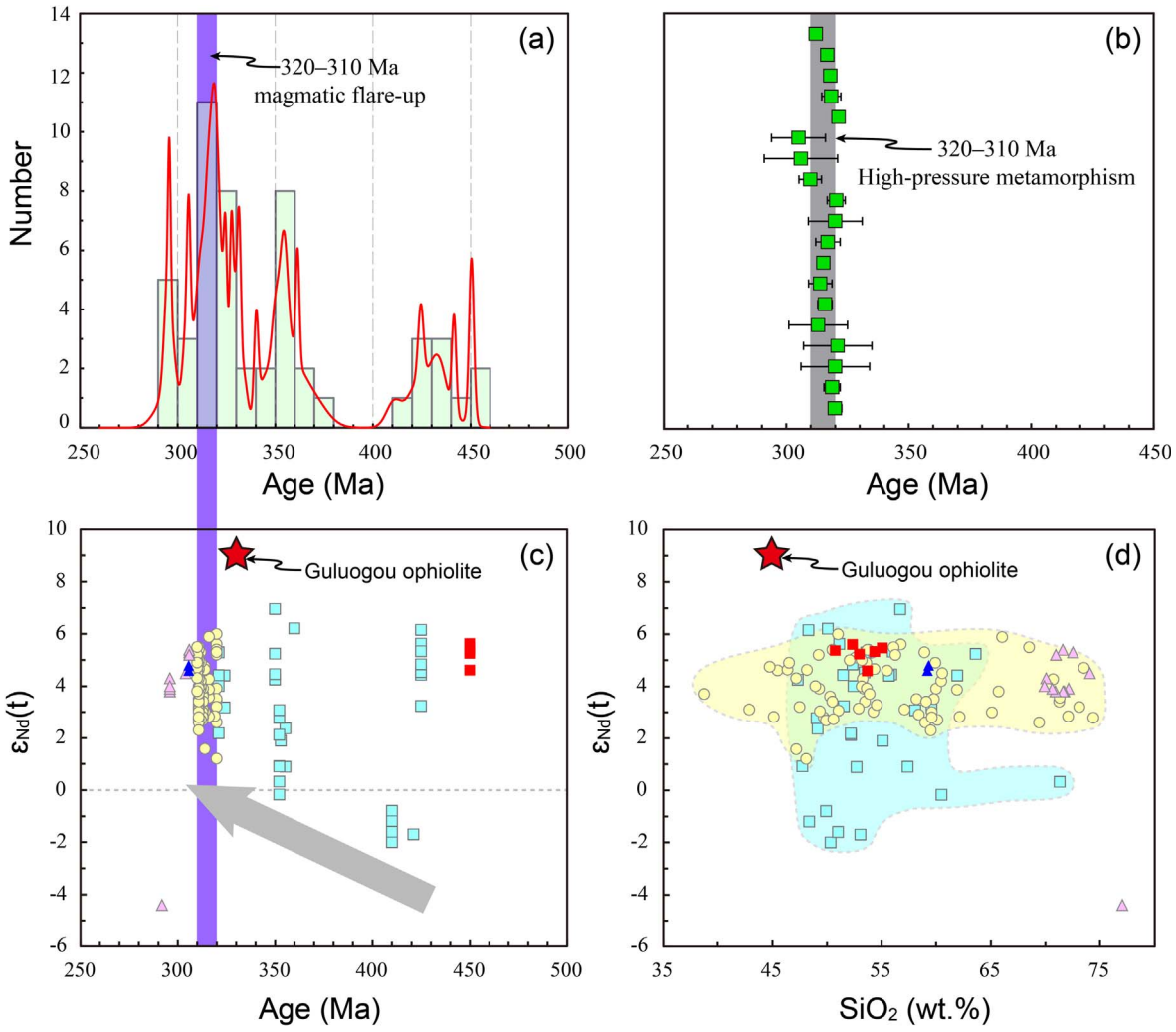


**Fig. 9.** (a) Histograms of zircon U–Pb ages for the Paleozoic (450–290 Ma) igneous rocks in the Awulale and adjacent areas of the Chinese Western Tianshan (see data sources in Table 2). (b) Compilation of peak eclogite-facies metamorphic ages for the Akeyazi high-pressure rocks in the Southwestern Tianshan. Note that a restricted range of ca. 320–310 Ma is recognized from published ages determined by different high-resolution dating methods (see text for details). *Data sources:* Su et al. (2010), Klemd et al. (2011), Li et al. (2011), John et al. (2012), van der Straaten et al. (2012), Yang et al. (2013), Du et al. (2014), Liu et al. (2014), Soldner et al. (2017) and Tan et al. (2017). (c) Whole-rock $\varepsilon_{Nd}(t)$ plotted as the function of crystallization ages for the Paleozoic rocks. (d) Plot of whole-rock $\varepsilon_{Nd}(t)$ vs. $SiO_2$ for the Paleozoic rocks. Data source are in Table S3. The red star represents the average whole-rock $\varepsilon_{Nd}(t)$ value (+9) of the N-MORB-type basalts from the ca. 333 Ma Gulugou ophiolite in the South Central Tianshan Suture Zone (Jiang et al., 2014a). Symbols as in Fig. 5. (For interpretation of the references to colour in this figure legend, the reader is referred to the web version of this article.)

(Fig. 10a). By inference, the 309–290 Ma magmatic rocks might be generated in a post-collisional setting subsequent to subduction-collision due to slab breakoff (Fig. 10c).

Exclusively, the iron deposits of AIMB in the Chinese Western Tianshan are hosted in the submarine volcanic-sedimentary rock associations of Dahalajunshan Formation. The rock associations are widespread without prominent regional metamorphism throughout the Yili-Central Tianshan Block and documented as a prolonged extrusive magmatism during late Devonian to late Carboniferous (ca. 370–300 Ma) based on numerous geochronological studies (e.g., Zhu et al., 2005, 2009; Yu et al., 2016). However, the mineralization ages of these submarine volcanic-hosted iron deposits are constrained in a short period of ca. 330–313 Ma by zircon U–Pb dating of ore-bearing volcanic rocks and Sm–Nd isochrons of skarns (Hong et al., 2012; Zhang et al., 2012, 2015; Li et al., 2013, 2015b; Duan et al., 2014). Taking the analytical errors into consideration, the ages of iron mineralization are distinctively bracketed in the ca. 320–310 Ma magmatic flare-up and peak eclogite-facies metamorphism, which is believed to be the result of slab breakoff in this study (Fig. 10b). Thus, we suggest slab breakoff as the exact tectonic setting during the generation of the submarine volcanic-hosted iron deposits in AIMB of the Chinese Western Tianshan.

### 5.3. Metallogenic implications

The intensively studied Zhibo and Chagangnuoer iron deposits in the AIMB share broadly similar geological characteristics to Kiruna- and IOCG-type iron deposits and the Chilean Iron Belt, including ore mineralization, ore textures, ore bodies structures and magnetite $\delta^{18}O$ values (Jiang et al., 2014b; Zhang et al., 2015). This is further supported by the ortho-magmatic trace element signatures and $\delta^{56}Fe$ values of magnetites, suggesting a close association with igneous rocks and magmatic-hydrothermal fluids (Richards and Mumin, 2013; Günther et al., 2017; Richards et al., 2017). Recently, Richards et al. (2017) suggest contrasting models for the formation of IOCG and porphyry deposits in the Mesozoic Coastal Cordillera of Chile due to the differences in tectonic setting and sulfur content of mineralization-related magmas. The IOCG deposits are thought to be formed from relatively sulfur poor magmas with somewhat isotopically primitive in composition in back-arc extensional settings during mid-Cretaceous in northern Chile (Richards et al., 2017). We hypothesize that this is likely the case for the submarine volcanic-hosted iron deposits in the Chinese Western Tianshan, where an extensional regime was dominated from subduction to post-collisional stages during late Paleozoic times.

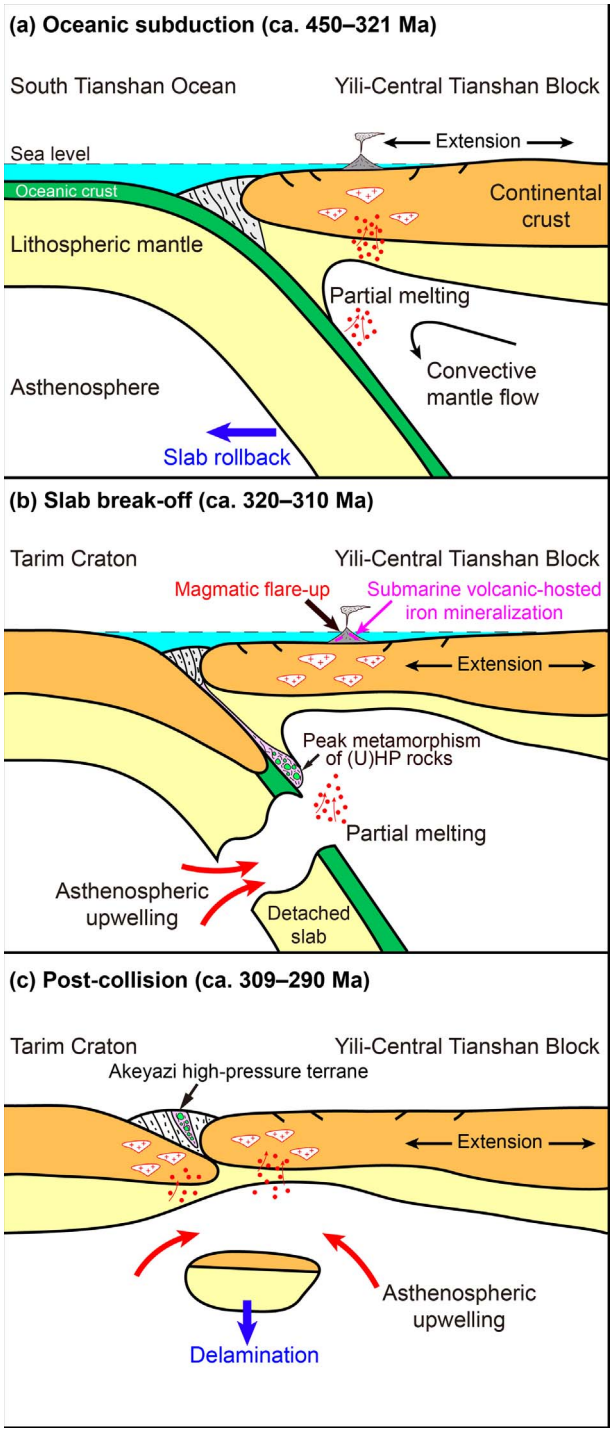


**Fig. 10.** Schematic model illustrating the Paleozoic (ca. 450–290 Ma) tectonic evolution of the Chinese Southwestern Tianshan from the northward subduction of the South Tianshan Ocean to the collision between the Tarim Craton and the Yili-Central Tianshan Block. Note that the submarine volcanic-hosted iron mineralization is synchronous with the ca. 320–310 Ma magmatic flare-up and peak metamorphism of the Akeyazi high-pressure terrane in the Chinese Western Tianshan.

However, it is noteworthy that the submarine volcanic-hosted iron deposits in the AIMB exclusively formed in a short time span of ca. 320–310 Ma intimately associated with slab breakoff (Fig. 10b).

The ca. 320–310 Ma ore-bearing volcanic rocks are characterized by scattered $SiO_2$ contents (basaltic-intermediate-felsic) and highly positive $\varepsilon_{Nd}(t)$ values (Fig. 9d) and they are interpreted as the result of continuous crystal fractionation of a common parental basaltic magma during ascent from its mantle source to the upper crust (Zhang et al., 2016). The basaltic magma derived from partial melting of subduction-modified depleted mantle wedge is generally iron rich, as exemplified by the ferrobasalts in the Chagangnuoer iron deposit (Li et al., 2015b), which is thought to be the most probable iron source for these submarine volcanic-hosted iron deposits in the AIMB. In addition, differentiation of the basaltic magma with relatively low water contents (usually with low oxygen fugacity; e.g., Kelley and Cottrell, 2009; Zimmer et al., 2010) is favorable for iron enrichment in the evolved melt and exsolution of iron-rich magmatic-hydrothermal fluids in the magma chamber since low oxygen fugacity will lead to suppression of Fe-Ti oxides fractionation (e.g., Sisson and Grove, 1993; Zimmer et al., 2010; Zhang et al., 2014c). Subsequently, release of the iron-rich fluids triggered by the sudden decompression associated with slab breakoff results in iron mineralization and relevant wall-rock alteration of the submarine volcanic-hosted iron deposits in the AIMB (Zhang et al., 2014c, 2016).

In the northwestern segment of the Chinese Western Tianshan, numerous porphyry copper–molybdenum and epithermal gold deposits are distributed in the Biezhentao and Borohoro areas, including Lamasu, Dabate, Kekesai, Lailisigao'er Cu–(Mo) deposits and Yiermande, Jingxi, Axi, Taerbieke Au deposits, which constituent an important Cu–Mo–Au metallogenic belt in Xinjiang (Tang et al., 2010). All these deposits were formed during the late Devonian–late Carboniferous (ca. 366–316 Ma) in association with contemporary magmatic rocks (Tang et al., 2010). Currently, extensive studies have well established that arc magmas with potential to form porphyry Cu–Mo–Au deposits are generated optimally under contractional conditions of overriding plate, as exemplified by the late Cretaceous and Eocene–Oligocene porphyry copper belts in northern Chile (Sillitoe, 2010; Richards et al., 2017). Therefore, although the Biezhentao–Borohoro Cu–Mo–Au metallogenic belt seems likely the northwestern extension of the Awulale Iron Metallogenic Belt, we interpret that they are formed in contrasting tectonic regimes.

The Biezhentao–Borohoro Cu–Mo–Au metallogenic belt is interpreted to be associated with the south-subduction of the North Tianshan Ocean and regarded as the eastern extension of the porphyry Cu belt in Central Kazakhstan, including Koksai, Borly, Kounrad and Aktogai deposits. The Cu–Mo–Au mineralization was developed during the construction of the late Devonian to Carboniferous Balkhash–Yili continental arc (Tang et al., 2010; Cao et al., 2016). In contrast, the AIMB was generated during slab breakoff subsequent to the northward-subduction termination of the South Tianshan Ocean under an extensional regime, which is inconsistent with the proposed southward subduction of the North Tianshan Ocean responsible for the Paleozoic magmatism in the Awulale and adjacent areas. In this regard, distinctive ore deposit types could be employed to provide additional constraints on the tectonic evolution of orogenic belts. Furthermore, the extensional regime in the southern Yili-Central Tianshan Block was dominated from subduction to post-collisional stages, which is not favorable for porphyry Cu–Mo–Au mineralization. Thus, we propose that the western extension of the AIMB parallel to the South Central Tianshan Suture Zone might be the most potential for prospecting submarine volcanic-hosted iron deposits in future.

## 6. Conclusions

By studying the Paleozoic (ca. 450–290 Ma) igneous rocks, which occurred in relatively close temporal and spatial proximity to the Awulale Iron Metallogenic Belt (AIMB) of the Chinese Western Tianshan, we showed that all magmatic rocks with broadly similar arc geochemical signatures were generated in an extensional regime. On the basis of the distinctive whole-rock Nd isotopic compositions and ca. 320–310 Ma peak eclogite-facies subduction-zone metamorphism of the Akeyazi high-pressure rocks, the Paleozoic igneous rocks are subdivided into three groups: (1) ca. 450–321 Ma with increasingly positive $\varepsilon_{Nd}(t)$ excursions, related to slab rollback during northward

subduction of the South Tianshan Ocean; (2) ca. 320–310 Ma magmatic flare-up with largely positive $\varepsilon_{Nd}(t)$ values, related to slab breakoff during tectonic transition; and (3) ca. 309–290 Ma, related to post-collision in the intracontinental setting. Exclusively, the mineralization ages of the submarine volcanic-hosted iron deposits in the AIMB are broadly bracketed in the ca. 320–310 Ma magmatic flare-up and peak eclogite-facies metamorphism, which enables us to propose a slab-breakoff model responsible for the iron mineralization. Finally, contrasting in the tectonic regime with the Biezhentao–Borohoro porphyry Cu–Mo–Au metallogenic belt in the northwestern Tianshan, the western extension of the AIMB parallel to the South Tianshan has significant potential for exploration of submarine volcanic-hosted iron deposits.

## Acknowledgements

This work was funded by National Key R&D Program of China (2017YFC0601206), the National Natural Science Foundation of China (41390445, 41025008), the China Postdoctoral Science Foundation (2016M600127), and the CSC-DAAD Postdoc Scholarship Program to Xin-Shui Wang. Special thanks to L. Su and H.Y. Zhang for assistance with LA-ICP-MS zircon U–Pb analyses and D.S. Xue and B.Y Gao for help with the whole-rock elemental analyses. We are also grateful to Prof. Reiner Klemd for insightful discussions and improving the English of the manuscript. We appreciate constructive comments by Associated Editor David Huston, Grant Cox and an anonymous reviewer that greatly improved the final version of the manuscript. Editor-in-Chief Franco Pirajno is thanked for editorial handling of this manuscript.

## Appendix A. Supplementary data

Supplementary data associated with this article can be found, in the online version, at http://dx.doi.org/10.1016/j.oregeorev.2017.11.015.

## References

Agard, P., Yamato, P., Jolivet, L., Burov, E., 2009. Exhumation of oceanic blueschists and eclogites in subduction zones: timing and mechanisms. Earth Sci. Rev. 92, 53–79.
Cao, M.J., Li, G.M., Qin, K.Z., Evans, N.J., Seitmuratova, E.Y., 2016. Assessing the magmatic affinity and petrogenesis of granitoids at the giant Aktogai porphyry Cu deposit, Central Kazakhstan. Am. J. Sci. 316, 614–668.
Castillo, P.R., Janney, P.E., Solidum, R.U., 1999. Petrology and geochemistry of Camiguin Island, southern Philippines: insights to the source of adakites and other lavas in a complex arc setting. Contrib. Miner. Petrol. 134, 33–51.
Chappell, B.W., White, A.J.R., 1992. I- and S-type granites in the Lachlan Fold Belt. Trans. R. Soc. Edinburgh Earth Sci. 83, 1–26.
Charvet, J., Shu, L.S., Laurent-Charvet, S., Wang, B., Faure, M., Cluzel, D., Chen, Y., De Jong, K., 2011. Palaeozoic tectonic evolution of the Tianshan belt, NW China. Sci. China: Earth Sci. 54, 166–184.
Chiaradia, M., 2015. Crustal thickness control on Sr/Y signatures of recent arc magmas: an Earth scale perspective. Sci. Rep. 5, 8115.
Collins, W.J., Belousova, E.A., Kemp, A.I., Murphy, J.B., 2011. Two contrasting Phanerozoic orogenic systems revealed by hafnium isotope data. Nat. Geosci. 4, 333–337.
Corfu, F., Hanchar, J.M., Hoskin, P.W.O., Kinny, P., 2003. Atlas of zircon textures. Rev. Mineral. Geochem. 53, 469–500.
Currie, C.A., Huismans, R.S., Beaumont, C., 2008. Thinning of continental backarc lithosphere by flow-induced gravitational instability. Earth Planet. Sci. Lett. 269, 436–447.
Dare, S.A.S., Barnes, S.J., Beaudoin, G., Méric, J., Boutroy, E., Potvin-Doucet, C., 2014. Trace elements in magnetite as petrogenetic indicators. Miner. Deposita 49, 785–796.
Davies, J.H., von Blanckenburg, F., 1995. Slab breakoff: a model of lithosphere detachment and its test in the magmatism and deformation of collisional orogens. Earth Planet. Sci. Lett. 129, 85–102.
Dong, Y.P., Zhang, G.W., Neubauer, F., Liu, X.M., Hauzenberger, C., Zhou, D.W., Li, W., 2011. Syn- and post-collisional granitoids in the Central Tianshan orogen: geochemistry, geochronology and implications for tectonic evolution. Gondwana Res. 20, 568–581.
Du, J.X., Zhang, L.F., Shen, X.J., Bader, T., 2014. A new P-T–t path of eclogites from Chinese southwestern Tianshan: constraints from P–T pseudosections and Sm–Nd isochron dating. Lithos 200, 258–272.
Duan, S.G., Zhang, Z.H., Jiang, Z.S., Zhao, J., Zhang, Y.P., Li, F.M., Tian, J.Q., 2014. Geology, geochemistry, and geochronology of the Dunde iron–zinc ore deposit in western Tianshan, China. Ore Geol. Rev. 57, 441–461.
Fiannacca, P., Cirrincione, R., Bonanno, F., Carciotto, M.M., 2015. Source-inherited compositional diversity in granite batholiths: the geochemical message of Late Paleozoic intrusive magmatism in central Calabria (southern Italy). Lithos 236, 123–140.
Frost, B.R., Barnes, C.G., Collins, W.J., Arculus, R.J., Ellis, D.J., Frost, C.D., 2001. A geochemical classification for granitic rocks. J. Petrol. 42, 2033–2048.
Frost, B.R., Frost, C.D., 2008. A geochemical classification for feldspathic igneous rocks. J. Petrol. 49, 1955–1969.
Furman, T., Graham, D., 1999. Erosion of lithospheric mantle beneath the East African Rift system: geochemical evidence from the Kivu volcanic province. Lithos 48, 237–262.
Günther, T., Klemd, R., Zhang, X., Horn, I., Weyer, S., 2017. In-situ trace element and Fe-isotope studies on magnetite of the volcanic-hosted Zhibo and Chagangnuoer iron ore deposits in the Western Tianshan, NW China. Chem. Geol. 453, 111–127.
Gao, J., Klemd, R., 2003. Formation of HP–LT rocks and their tectonic implications in the western Tianshan Orogen, NW China: geochemical and age constraints. Lithos 66, 1–22.
Gao, J., Klemd, R., Qian, Q., Zhang, X., Li, J.L., Jiang, T., Yang, Y.Q., 2011. The collision between the Yili and Tarim blocks of the Southwestern Altaids: geochemical and age constraints of a leucogranite dike crosscutting the HP–LT metamorphic belt in the Chinese Tianshan Orogen. Tectonophysics 499, 118–131.
Gao, J., Li, M.S., Xiao, X.C., Tang, Y.Q., He, G.Q., 1998. Paleozoic tectonic evolution of the Tianshan Orogen, northwestern China. Tectonophysics 287, 213–231.
Gao, J., Long, L.L., Klemd, R., Qian, Q., Liu, D.Y., Xiong, X.M., Su, W., Liu, W., Wang, Y.T., Yang, F.Q., 2009. Tectonic evolution of the South Tianshan orogen and adjacent regions, NW China: geochemical and age constraints of granitoid rocks. Int. J. Earth Sci. 98, 1221–1238.
Gao, J., Wang, X.S., Klemd, R., Jiang, T., Qian, Q., Mu, L.X., Ma, Y.Z., 2015. Record of assembly and breakup of Rodinia in the Southwestern Altaids: evidence from Neoproterozoic magmatism in the Chinese Western Tianshan Orogen. J. Asian Earth Sci. 113, 173–193.
Ge, S.S., Zhai, M.G., Safonova, I., Li, D.P., Zhu, X., Zuo, P.F., Shan, H.X., 2015. Whole-rock geochemistry and Sr–Nd–Pb isotope systematics of the Late Carboniferous volcanic rocks of the Awulale metallogenic belt in the western Tianshan Mountains (NW China): petrogenesis and geodynamical implications. Lithos 228, 62–77.
Green, T.H., Ringwood, A.E., 1968. Genesis of the calc-alkaline igneous rock suite. Contrib. Miner. Petrol. 18, 105–162.
Hacker, B.R., Gerya, T.V., 2013. Paradigms, new and old, for ultrahigh-pressure tectonism. Tectonophysics 603, 79–88.
Han, B.F., Guo, Z.J., Zhang, Z.C., Zhang, L., Chen, J.F., Song, B., 2010. Age, geochemistry, and tectonic implications of a late Paleozoic stitching pluton in the North Tian Shan suture zone, western China. Geol. Soc. Am. Bull. 122, 627–640.
Han, B.F., He, G.Q., Wang, X.C., Guo, Z.J., 2011. Late Carboniferous collision between the Tarim and Kazakhstan-Yili terranes in the western segment of the South Tian Shan Orogen, Central Asia, and implications for the Northern Xinjiang, western China. Earth Sci. Rev. 109, 74–93.
Henriquez, F., Martin, R.F., 1978. Crystal-growth textures in magnetite flows and feeder dykes, El Laco, Chile. Can. Mineral. 16, 581–589.
Hong, W., Zhang, Z.H., Li, H.Q., Li, F.M., Liu, X.Z., 2012. Metallogenic epoch of Chagangnuoer iron deposit in western Tianshan Mountains, Xinjiang: information from garnet Sm–Nd isochron age. Miner. Deposits 31, 1067–1074 (in Chinese with English abstract).
Hou, T., Zhang, Z.C., Pirajno, F., Santosh, M., Encarnacion, J., Liu, J.L., Zhao, Z., Zhang, L.J., 2014. Geology, tectonic settings and iron ore metallogenesis associated with submarine volcanism in China: An overview. Ore Geol. Rev. 57, 498–517.
Jiang, T., Gao, J., Klemd, R., Qian, Q., Zhang, X., Xiong, X.M., Wang, X.S., Tan, Z., Chen, B.X., 2014a. Paleozoic ophiolitic mélanges from the South Tianshan Orogen, NW China: Geological, geochemical and geochronological implications for the geodynamic setting. Tectonophysics 612, 106–127.
Jiang, Z.S., Zhang, Z.H., Wang, Z.H., Duan, S.G., Li, F.M., Tian, J.Q., 2014b. Geology, geochemistry, and geochronology of the Zhibo iron deposit in the Western Tianshan, NW China: Constraints on metallogenesis and tectonic setting. Ore Geol. Rev. 57, 406–424.
John, T., Gussone, N., Podladchikov, Y.Y., Bebout, G.E., Dohmen, R., Halama, R., Klemd, R., Magna, T., Seitz, H.M., 2012. Volcanic arcs fed by rapid pulsed fluid flow through subducting slabs. Nat. Geosci. 5, 489–492.
Keller, C.B., Schoene, B., Barboni, M., Samperton, K.M., Husson, J.M., 2015. Volcanic-plutonic parity and the differentiation of the continental crust. Nature 523, 301–307.
Kelley, K.A., Cottrell, E., 2009. Water and the oxidation state of subduction zone magmas. Science 325, 605–607.
Klemd, R., Bröcker, M., Hacker, B.R., Gao, J., Gans, P., Wemmer, K., 2005. New age constraints on the metamorphic evolution of the high-pressure/low-temperature belt in the Western Tianshan Mountains, NW China. J. Geol. 113, 157–168.
Klemd, R., Gao, J., Li, J.L., Meyer, M., 2015. Metamorphic evolution of (ultra)-high-pressure subduction-related transient crust in the South Tianshan Orogen (Central Asian Orogenic Belt): Geodynamic implications. Gondwana Res. 28, 1–25.
Klemd, R., John, T., Scherer, E.E., Rondenay, S., Gao, J., 2011. Changes in dip of subducted slabs at depth: Petrological and geochronological evidence from HP–UHP rocks (Tianshan, NW-China). Earth Planet. Sci. Lett. 310, 9–20.
Kröner, A., Windley, B.F., Badarch, G., Tomurtogoo, O., Hegner, E., Jahn, B.M., Gruschka, S., Khain, E.V., Demoux, A., Wingate, M.T.D., 2007. Accretionary growth and crust formation in the Central Asian Orogenic Belt and comparison with the Arabian-Nubian shield. Geological Society of America Memoirs 200, 181–209.
Le Bas, M.J., Le Maitre, R.W., Streckeisen, A., Zanettin, B., 1986. A chemical classification of volcanic rocks based on the total alkali-silica diagram. J. Petrol. 27, 745–750.
Lee, C.T.A., Bachmann, O., 2014. How important is the role of crystal fractionation in making intermediate magmas? Insights from Zr and P systematics. Earth Planet. Sci. Lett. 393, 266–274.

Lee, C.T.A., Morton, D.M., 2015. High silica granites: Terminal porosity and crystal settling in shallow magma chambers. Earth Planet. Sci. Lett. 409, 23–31.
Lee, C.T.A., Morton, D.M., Kistler, R.W., Baird, A.K., 2007. Petrology and tectonics of Phanerozoic continent formation: From island arcs to accretion and continental arc magmatism. Earth Planet. Sci. Lett. 263, 370–387.
Li, C., Xiao, W.J., Han, C.M., Zhou, K.F., Zhang, J.E., Zhang, Z.X., 2015a. Late Devonian–early Permian accretionary orogenesis along the North Tianshan in the southern Central Asian Orogenic Belt. International Geology Review 57, 1023–1050.
Li, D.P., Du, Y.S., Pang, Z.S., Tu, Q.J., Zhang, Y.P., Ge, S.S., Sheng, L.J., Wang, K.H., 2013. Zircon U-Pb chronology and geochemistry of Carboniferous volcanic rocks in Awulale area, Western Tianshan Mountains. Acta Geoscientica Sinica 34, 176–192 (in Chinese with English abstract).
Li, J.L., Gao, J., Wang, X.S., 2016. A subduction channel model for exhumation of oceanic-type high-pressure to ultrahigh-pressure eclogite-facies metamorphic rocks in SW Tianshan, China. Science China Earth Sciences 59, 2339–2354.
Li, N.B., Niu, H.C., Zhang, X.C., Zeng, Q.S., Shan, Q., Li, C.Y., Yan, S., Yang, W.B., 2015b. Age, petrogenesis and tectonic significance of the ferrobasalts in the Chagangnuoer iron deposit, western Tianshan. International Geology Review 1–21.
Li, N.B., Niu, H.C., Shan, Q., Yang, W.B., 2015c. Two episodes of Late Paleozoic A-type magmatism in the Qunjisayi area, western Tianshan: Petrogenesis and tectonic implications. J. Asian Earth Sci. 113, 238–253.
Li, Q.L., Lin, W., Su, W., Li, X.H., Shi, Y.H., Liu, Y., Tang, G.Q., 2011. SIMS U-Pb rutile age of low-temperature eclogites from southwestern Chinese Tianshan, NW China. Lithos 122, 76–86.
Liu, X., Su, W., Gao, J., Li, J.L., Jiang, T., Zhang, X., Ge, X.M., 2014. Paleozoic subduction erosion involving accretionary wedge sediments in the South Tianshan Orogen: Evidence from geochronological and geochemical studies on eclogites and their host metasediments. Lithos 210–211, 89–110.
Lomize, M.G., Demina, L.I., Zarshchikov, A.A., 1997. The Kyrgyz-Terskei Paleoceanic Basin, Tien Shan. Geotectonics 31, 463–482.
Long, L.L., Gao, J., Klemd, R., Beier, C., Qian, Q., Zhang, X., Wang, J.B., Jiang, T., 2011. Geochemical and geochronological studies of granitoid rocks from the Western Tianshan Orogen: Implications for continental growth in the southwestern Central Asian Orogenic Belt. Lithos 126, 321–340.
Ma, X.X., Shu, L.S., Santosh, M., Li, J.Y., 2012. Petrogenesis and tectonic significance of an early Palaeozoic mafic-intermediate suite of rocks from the Central Tianshan, northwest China. International Geology Review 55, 548–573.
Maniar, P.D., Piccoli, P.M., 1989. Tectonic discrimination of granitoids. Geol. Soc. Am. Bull. 101, 635–643.
Meyer, M., Klemd, R., Konopelko, D., 2013. High-pressure mafic oceanic rocks from the Makbal Complex, Tianshan Mountains (Kazakhstan & Kyrgyzstan): implications for the metamorphic evolution of a fossil subduction zone. Lithos 177, 207–225.
Miller, C., Schuster, R., Klötzli, U., Frank, W., Purtscheller, F., 1999. Post-Collisional Potassic and Ultrapotassic Magmatism in SW Tibet: Geochemical and Sr–Nd–Pb–O Isotopic Constraints for Mantle Source Characteristics and Petrogenesis. J. Petrol. 40, 1399–1424.
Nystroem, J.O., Henriquez, F., 1994. Magmatic features of iron ores of the Kiruna type in Chile and Sweden; ore textures and magnetite geochemistry. Econ. Geol. 89, 820–839.
Nystroem, J.O., Billström, K., Henríquez, F., Fallick, A.E., Naslund, H.R., 2008. Oxygen isotope composition of magnetite in iron ores of the Kiruna type in Chile and Sweden. GFF 130, 177–188.
Patiño Douce, A.E., 1999. What do experiments tell us about the relative contributions of crust and mantle to the origin of granitic magmas? Geological Society, London, Special Publications 168, 55–75.
Pearce, J.A., 2014. Immobile element fingerprinting of ophiolites. Elements 10, 101–108.
Pearce, J.A., Harris, N.B.W., Tindle, A.G., 1984. Trace element discrimination diagrams for the tectonic interpretation of granitic rocks. J. Petrol. 25, 956–983.
Peccerillo, A., Taylor, S.R., 1976. Geochemistry of eocene calc-alkaline volcanic rocks from the Kastamonu area, Northern Turkey. Contrib. Miner. Petrol. 58, 63–81.
Qian, Q., Gao, J., Klemd, R., He, G.Q., Song, B., Liu, D.Y., Xu, R.H., 2009. Early Paleozoic tectonic evolution of the Chinese South Tianshan Orogen: constraints from SHRIMP zircon U-Pb geochronology and geochemistry of basaltic and dioritic rocks from Xiate, NW China. Int. J. Earth Sci. 98, 551–569.
Rapp, R.P., Watson, E.B., 1995. Dehydration melting of metabasalt at 8–32 kbar: implications for continental growth and crust-mantle recycling. J. Petrol. 36, 891–931.
Richards, J.P., Kerrich, R., 2007. Adakite-like rocks: their diverse origins and questionable role in metallogenesis. Econ. Geol. 102, 537–576.
Richards, J.P., López, G.P., Zhu, J.-J., Creaser, R.A., Locock, A.J., Mumin, A.H., 2017. Contrasting Tectonic Settings and Sulfur Contents of Magmas Associated with Cretaceous Porphyry Cu ± Mo ± Au and Intrusion-Related Iron Oxide Cu-Au Deposits in Northern Chile. Econ. Geol. 112, 295–318.
Richards, J.P., Mumin, A.H., 2013. Magmatic-hydrothermal processes within an evolving Earth: Iron oxide-copper-gold and porphyry Cu ± Mo ± Au deposits. Geology 41, 767–770.
Sillitoe, R.H., 2010. Porphyry copper systems. Econ. Geol. 105, 3–41.
Sisson, T.W., Grove, T.L., 1993. Experimental investigations of the role of H2O in calc-alkaline differentiation and subduction zone magmatism. Contrib. Miner. Petrol. 113, 143–166.
Soldner, J., Oliot, E., Schulmann, K., Štípská, P., Kusbach, V., Anczkiewicz, R., 2017. Metamorphic P-T–t–d evolution of (U)HP metabasites from the South Tianshan accretionary complex (NW China) — Implications for rock deformation during exhumation in a subduction channel. Gondwana Res. 47, 161–187.
Sun, L.H., Wang, Y.J., Fan, W.M., Zi, J.W., 2008. Post-collisional potassic magmatism in the Southern Awulale Mountain, western Tianshan Orogen: Petrogenetic and tectonic implications. Gondwana Res. 14, 383–394.
Su, W., Gao, J., Klemd, R., Li, J.L., Zhang, X., Li, X.H., Chen, N.S., Zhang, L., 2010. U-Pb zircon geochronology of Tianshan eclogites in NW China: implication for the collision between the Yili and Tarim blocks of the southwestern Altaids. Eur. J. Mineral. 22, 473–478.
Sun, S.S., McDonough, W.F., 1989. Chemical and isotopic systematics of oceanic basalts: implications for mantle composition and processes. In: Saunders, A.D., Norry, M.J. (Eds.), Magmatism in the Ocean Basin. Geological Society of London Special Publications, pp. 313–345.
Tan, Z., Agard, P., Gao, J., John, T., Li, J.L., Jiang, T., Bayet, L., Wang, X.S., Zhang, X., 2017. P-T–time-isotopic evolution of coesite-bearing eclogites: Implications for exhumation processes in SW Tianshan. Lithos 278–281, 1–25.
Tang, G.J., Wang, Q., Wyman, D.A., Sun, M., Li, Z.X., Zhao, Z.H., Sun, W.D., Jia, X.H., Jiang, Z.Q., 2010. Geochronology and geochemistry of Late Paleozoic magmatic rocks in the Lamasu-Dabate area, northwestern Tianshan (west China): evidence for a tectonic transition from arc to post-collisional setting. Lithos 119, 393–411.
Tornos, F., Velasco, F., Hanchar, J.M., 2016. Iron-rich melts, magmatic magnetite, and superheated hydrothermal systems: The El Laco deposit, Chile. Geology 44, 427–430.
van der Straaten, F., Halama, R., John, T., Schenk, V., Hauff, F., Andersen, N., 2012. Tracing the effects of high-pressure metasomatic fluids and seawater alteration in blueschist-facies overprinted eclogites: Implications for subduction channel processes. Chem. Geol. 292–293, 69–87.
van Hunen, J., Allen, M.B., 2011. Continental collision and slab break-off: A comparison of 3-D numerical models with observations. Earth Planet. Sci. Lett. 302, 27–37.
Wakita, K., Pubellier, M., Windley, B.F., 2013. Tectonic processes, from rifting to collision via subduction, in SE Asia and the western Pacific: A key to understanding the architecture of the Central Asian Orogenic Belt. Lithosphere 5, 265–276.
Wan, B., Xiao, W.J., Windley, B.F., Gao, J., Zhang, L.C., Cai, K.D., 2017. Contrasting ore styles and their role in understanding the evolution of the Altaids. Ore Geol. Rev. 80, 910–922.
Wang, B., Faure, M., Cluzel, D., Shu, L.S., Charvet, J., Meffre, S., Ma, Q., 2006. Late Paleozoic tectonic evolution of the northern West Chinese Tianshan belt. Geodin. Acta 19, 237–247.
Wang, B., Faure, M., Shu, L.S., Cluzel, D., Charvet, J., De Jong, K., Chen, Y., 2008. Paleozoic tectonic evolution of the Yili Block, western Chinese Tianshan. Bull. Soc. Geol. Fr. 179, 483–490.
Wang, B., Jahn, B.M., Shu, L.S., Li, K.S., Chung, S.L., Liu, D.Y., 2012. Middle-Late Ordovician arc-type plutonism in the NW Chinese Tianshan: Implication for the accretion of the Kazakhstan continent in Central Asia. J. Asian Earth Sci. 49, 40–53.
Wang, B., Liu, H.S., Shu, L.S., Jahn, B.M., Chung, S.L., Zhai, Y.Z., Liu, D.Y., 2014a. Early Neoproterozoic crustal evolution in northern Yili Block: Insights from migmatite, orthogneiss and leucogranite of the Wenquan metamorphic complex in the NW Chinese Tianshan. Precambr. Res. 242, 58–81.
Wang, B., Shu, L.S., Cluzel, D., Faure, M., Charvet, J., 2007. Geochemical constraints on Carboniferous volcanic rocks of the Yili Block (Xinjiang, NW China): implication for the tectonic evolution of Western Tianshan. J. Asian Earth Sci. 29, 148–159.
Wang, B., Shu, L.S., Faure, M., Jahn, B.M., Cluzel, D., Charvet, J., Chung, S.L., Meffre, S., 2011a. Paleozoic tectonics of the southern Chinese Tianshan: Insights from structural, chronological and geochemical studies of the Heiyingshan ophiolitic mélange (NW China). Tectonophysics 497, 85–104.
Wang, B.Y., Hu, X.J., Wang, J.T., Shao, Q.H., Ling, J.L., Guo, N.X., Zhao, Y.F., Xia, Z.D., Jiang, C.Y., 2011b. Geological characteristics and genesis of Chagannur iron deposit in Western Tianshan, Xinjiang. Mineral Deposits 30, 385–402 (in Chinese with English abstract).
Wang, X.S., Gao, J., Klemd, R., Jiang, T., Li, J.L., Zhang, X., Tan, Z., Li, L., Zhu, Z.X., 2014b. Geochemistry and geochronology of the Precambrian high-grade metamorphic complex in the Southern Central Tianshan ophiolitic mélange, NW China. Precambr. Res. 254, 129–148.
Wang, X.S., Gao, J., Klemd, R., Jiang, T., Li, J.L., Zhang, X., Xue, S.C., 2017. The Central Tianshan Block: a microcontinent with a Neoarchean-Paleoproterozoic basement in the southwestern Central Asian Orogenic Belt. Precambr. Res. 295, 130–150.
Warren, C.J., 2013. Exhumation of (ultra-) high-pressure terranes: concepts and mechanisms. Solid Earth 4, 75–92.
Warren, C.J., Beaumont, C., Jamieson, R.A., 2008. Modelling tectonic styles and ultra-high pressure (UHP) rock exhumation during the transition from oceanic subduction to continental collision. Earth Planet. Sci. Lett. 267, 129–145.
Whalen, J.B., Currie, K.L., Chappell, B.W., 1987. A-type granites: geochemical characteristics, discrimination and petrogenesis. Contrib. Miner. Petrol. 95, 407–419.
Wilhem, C., Windley, B.F., Stampfli, G.M., 2012. The Altaids of Central Asia: a tectonic and evolutionary innovative review. Earth Sci. Rev. 113, 303–341.
Wolf, M.B., London, D., 1994. Apatite dissolution into peraluminous haplogranitic melts: an experimental study of solubilities and mechanisms. Geochim. Cosmochim. Acta 58, 4127–4145.
XBGMR, 1972a. 1:200000 Geological map of PRC, Xiaobulusitai sheet (K-45-VIII). National 543 Publishing House.
XBGMR, 1972b. 1:200000 Geological map of PRC, Bayinbuluke sheet (K-45-VII). National 543 Publishing House.
Xia, B., Zhang, L.F., Bader, T., 2014. Zircon U-Pb ages and Hf isotopic analyses of migmatite from the 'paired metamorphic belt' in Chinese SW Tianshan: constraints on partial melting associated with orogeny. Lithos 192–195, 158–179.
Xia, L.Q., Xu, X.Y., Xia, Z.C., Li, X.M., Ma, Z.P., Wang, L.S., 2004. Petrogenesis of Carboniferous rift-related volcanic rocks in the Tianshan, northwestern China. Geol. Soc. Am. Bull. 116, 419–433.
Xiao, W.J., Windley, B.F., Allen, M.B., Han, C.M., 2013. Paleozoic multiple accretionary and collisional tectonics of the Chinese Tianshan orogenic collage. Gondwana Res. 23, 1316–1341.
Xiao, W.J., Windley, B.F., Sun, S., Li, J.L., Huang, B.C., Han, C.M., Yuan, C., Sun, M.,

Chen, H.L., 2015. A tale of amalgamation of three Permo-Triassic collage systems in Central Asia: oroclines, sutures, and terminal accretion. Annu. Rev. Earth Planet. Sci. 43, 477–507.
Xing, H., Zhao, X.B., Zhang, Z.C., Ye, J.C., Feng, B., 2016. Early Paleozoic geological environment of metallogeny in Bavinbuluk region, western Tien Shan: igneous rocks and their dating, elementary and isotopic constraints. Acta Petrol. Sin. 32, 1770–1794 (in Chinese with English abstract).
Xiong, X.L., Adam, J., Green, T.H., 2005. Rutile stability and rutile/melt HFSE partitioning during partial melting of hydrous basalt: implications for TTG genesis. Chem. Geol. 218, 339–359.
Xu, X.Y., Li, X.M., Ma, Z.P., Xia, L.Q., Xia, Z.C., Peng, S.X., 2006. LA-ICPMS Zircon U-Pb Dating of Gabbro from the Bayingou Ophiolite in the Northern Tianshan Mountains. Acta Geol. Sinica 80, 1168–1176 (in Chinese with English abstract).
Xu, X.Y., Wang, H.L., Li, P., Chen, J.L., Ma, Z.P., Zhu, T., Wang, N., Dong, Y.P., 2013. Geochemistry and geochronology of Paleozoic intrusions in the Nalati (Narati) area in western Tianshan, Xinjiang, China: implications for Paleozoic tectonic evolution. J. Asian Earth Sci. 72, 33–62.
Yakubchuk, A., 2004. Architecture and mineral deposit settings of the Altaid orogenic collage: a revised model. J. Asian Earth Sci. 23, 761–779.
Yan, S., Shan, Q., Niu, H.C., Yang, W.B., Li, N.B., Zeng, L.J., Jiang, Y.H., 2015. Petrology and geochemistry of late Carboniferous hornblende gabbro from the Awulale Mountains, western Tianshan (NW China): implication for an arc–nascent back-arc environment. J. Asian Earth Sci. 113, 218–237.
Yang, W.B., Niu, H.C., Shan, Q., Luo, Y., Sun, W.D., Li, C.Y., Li, N.B., Yu, X.Y., 2012. Late Paleozoic calc-alkaline to shoshonitic magmatism and its geodynamic implications, Yuximolegai area, western Tianshan, Xinjiang. Gondwana Res. 22, 325–340.
Yang, X., Zhang, L.F., Tian, Z.L., Bader, T., 2013. Petrology and U-Pb zircon dating of coesite-bearing metapelite from the Kebuerte Valley, western Tianshan, China. J. Asian Earth Sci. 70–71, 295–307.
Yu, X.Q., Wang, Z.X., Zhou, X., Xiao, W.F., Yang, X.P., 2016. Zircon U-Pb geochronology and Sr–Nd isotopes of volcanic rocks from the Dahalajunshan Formation: implications for Late Devonian-Middle Carboniferous tectonic evolution of the Chinese Western Tianshan. Int. J. Earth Sci. 105, 1637–1661.
Zhang, X., Gao, J., Dong, L.H., Li, J.L., Jiang, T., Qian, Q., Su, W., 2011. Zircon LA-ICP-MS U-Pb ages of I type granitoids from Qiaohuote copper deposit in Central Tianshan of Xinjiang and its geological implications. Acta Petrol. Sin. 27, 1637–1648 (in Chinese with English abstract).
Zhang, X., Klemd, R., Gao, J., Dong, L.H., Wang, X.S., Haase, K., Jiang, T., Qian, Q., 2015. Metallogenesis of the Zhibo and Chagangnuoer volcanic iron oxide deposits in the Awulale Iron Metallogenic Belt, Western Tianshan orogen, China. J. Asian Earth Sci. 113, 151–172.
Zhang, X., Tian, J.Q., Gao, J., Klemd, R., Dong, L.H., Fan, J.J., Jiang, T., Hu, C.J., Qian, Q., 2012. Geochronology and geochemistry of granitoid rocks from the Zhibo syngenetic volcanogenic iron ore deposit in the Western Tianshan Mountains (NW-China): constraints on the age of mineralization and tectonic setting. Gondwana Res. 22, 585–596.
Zhang, Z.C., Hou, T., Santosh, M., Li, H.M., Li, J.W., Zhang, Z.H., Song, X.Y., Wang, M., 2014a. Spatio-temporal distribution and tectonic settings of the major iron deposits in China: an overview. Ore Geol. Rev. 57, 247–263.
Zhang, Z.C., Chai, F.M., Xie, Q.H., 2016. High-angle subduction in a thermal structure with warm mantle-cool crust: formation of submarine volcanics-hosted iron deposits. Geol. China 43 (2), 367–379 (in Chinese with English abstract).
Zhang, Z.C., et al., 2014c. Enrichment mechanism of iron in magmatic-hydrothermal system. Acta Petrol. Sin. 30 (5), 1189–1204 (in Chinese with English abstract).
Zhang, Z.H., Hong, W., Jiang, Z.S., Duan, S.G., Li, F.M., Shi, F.P., 2014b. Geological characteristics and metallogenesis of iron deposits in western Tianshan, China. Ore Geol. Rev. 57, 425–440.
Zhong, L.L., Wang, B., Alexeiev, D.V., Cao, Y.C., Biske, Y.S., Liu, H.S., Zhai, Y.Z., Xing, L.Z., 2017. Paleozoic multi-stage accretionary evolution of the SW Chinese Tianshan: new constraints from plutonic complex in the Nalati Range. Gondwana Res. 45, 254–274.
Zhu, D.C., Wang, Q., Zhao, Z.D., Chung, S.L., Cawood, P.A., Niu, Y.L., Liu, S.A., Wu, F.Y., Mo, X.X., 2015. Magmatic record of India-Asia collision. Sci. Rep. 5, 14289 Doi: 14210.11038/srep14289.
Zhu, T., Ma, Z.P., Xu, X.Y., Wang, H.L., Chen, J.L., Tang, Z., Sun, J.M., 2012. Geochemical and geochronlogical studies of Dagete diorite in Nalati magmatic belt of Middle Tianshan Mountains. Geol. Bull. China 31, 1965–1972 (in Chinese with English abstract).
Zhu, Y.F., Guo, X., Song, B., Zhang, L.F., Gu, L.B., 2009. Petrology, Sr–Nd–Hf isotopic geochemistry and zircon chronology of the Late Palaeozoic volcanic rocks in the southwestern Tianshan Mountains, Xinjiang, NW China. J. Geol. Soc. 166, 1085–1099.
Zhu, Y.F., Zhang, L.F., Gu, L.B., Guo, X., Zhou, J., 2005. The zircon SHRIMP chronology and trace element geochemistry of the Carboniferous volcanic rocks in western Tianshan Mountains. Chin. Sci. Bull. 50, 2201–2212.
Zhu, Z.X., Wang, K.Z., Zheng, Y.J., Sun, G.H., Zhang, C., Li, Y.P., 2006. Zircon SHRIMP dating of Silurian and Devonian granitic intrusions in the southern YiIi block, Xinjiang and preliminary discussion on their tectonic setting. Acta Petrol. Sin. 22, 1193–1200 (In Chinese with English abstract).
Zimmer, M.M., Plank, T., Hauri, E.H., Yogodzinski, G.M., Stelling, P., Larsen, J., Singer, B., Jicha, B., Mandeville, C., Nye, C.J., 2010. The role of water in generating the calc-alkaline trend: new volatile data for Aleutian magmas and a new tholeiitic index. J. Petrol. 51, 2411–2444.